

1D Radiation Analysis for
the Fusion Ignition Experiment
ZEPHYR

H.Brockmann^{+) , H.Krause, U.Ohlig^{+))}}

IPP 1/173

Nov. 79



MAX-PLANCK-INSTITUT FÜR PLASMAPHYSIK

8046 GARCHING BEI MÜNCHEN

MAX-PLANCK-INSTITUT FÜR PLASMAPHYSIK

GARCHING BEI MÜNCHEN

1D Radiation Analysis for the Fusion Ignition Experiment ZEPHYR

H.Brockmann^{+) , H.Krause, U.Ohlig^{+))}}

IPP 1/173

Nov. 79

^{+))} Institut für Reaktorentwicklung
Kernforschungsanlage Jülich GmbH,
Assoziation EURATOM-KFA

*Die nachstehende Arbeit wurde im Rahmen des Vertrages zwischen dem
Max-Planck-Institut für Plasmaphysik und der Europäischen Atomgemeinschaft über die
Zusammenarbeit auf dem Gebiete der Plasmaphysik durchgeführt.*

Abstract

For the proposed tokamak ignition experiment ZEPHYR a nuclear radiation analysis is performed for both the prompt radiation during a discharge and the delayed radiation after discharges. This analysis is restricted to a one-dimensional geometrical approximation of the apparatus. Nuclear heating data are derived for the prompt radiation and the shielding concept is investigated. Results for the delayed radiation are given for three activation scenarios, that are anticipated for machine operation. The cooling phase after one of these scenarios is investigated in some detail in order to trace the dominant contributions to biological dose rates back to machine components and to specific activation reactions.

5. Conclusion 41

References 41

Appendix A 43

Appendix B 44

⁺) Institut für Reaktorentwicklung
Kernforschungsanlage Jülich GmbH
Assoziation EURATOM-KFA

Contents

	page
1. Introduction	1
2.1 The experiment ZEPHYR	2
2.2 The geometry of the 1D radiation transport model	5
2.3 Prompt radiation transport: codes and cross-sections	10
2.4 Prompt radiation: energy deposition	11
2.5 Prompt radiation: biological dose rates	15
2.6 Prompt biological dose rates for deuterium operation	18
3.1 Delayed gamma-ray transport: codes and cross sections	19
3.2 Activation after final shutdown	20
3.3 Delayed radiation: biological dose rates	28
4. Delayed radiation after 10 days of DT-pulsing	35
5. Delayed radiation after one year of deuterium pulsing	37
6. Conclusions	41
References	41
Appendix A Materials	43
Appendix B Activation reactions and decay chains	44

*) Ignition experiment for the physics in a reactor

**) In cooperation with MIT, Cambridge, USA and Division Enrico Fermi, Frascati, Italy

1. Introduction

Plasma physics has proceeded at such a pace in recent years, that the planning of tokamak experiments which will achieve ignition is pursued now with some confidence into plasma physical scaling laws. The word "ignition" is used here to describe the plasma state, where thermonuclear fusion reactions release sufficient energy in the plasma to balance all energy losses.

One of these experiments to investigate ignited plasmas is ZEPHYR ("Zünd-Experiment für die Physik im Reaktor"^{+)) being designed at the Max-Planck-Institut für Plasmaphysik⁺⁺⁾ in Garching. Using a deuterium-tritium mixture as fuel ignition will be achieved by the well-known reaction $T + D \rightarrow He^4 + n + 17.6 \text{ MeV}$, which releases one 14.1 MeV neutron for each fusion reaction. Thus for the duration of an ignited discharge the plasma emits a large number of high energy neutrons which require a very significant effort to shield people and plasma diagnostics from its deleterious effects. In addition, the neutrons cause severe activation of the experiment and its surroundings. This delayed radiation makes personal access after shutdown difficult or impossible depending on the specific workplace in view and on the discharge history preceding.}

Thus, the radiation problem will have a strong impact on the experiment and radiation calculations are required to assist in machine designing to determine remote-handling requirements and to lay-out the radiation shields.

This report summarizes results of a set of one-dimensional radiation transport calculations which treat both the prompt radiation

^{+))} ignition experiment for the physics in a reactor

⁺⁺⁾ in cooperation with MIT, Cambridge, USA and
Divisione Fusione of CNEN, Frascati, Italy

(during a discharge) and the delayed radiation (after a sequence of discharges). The following chapter gives a short description of ZEPHYR as far as it is of significance to the radiation problem. The next two chapters deal with the 1D-model and the radiation transport code used for approximating a complex three-dimensional toroidal arrangement. The next group of chapters describes the conditions prevailing during a discharge. Both ignited DT-discharges are treated and discharges with pure deuterium filling. In the last set of chapters the γ -activation of the experiment after various discharge sequences is analysed and biological dose rates for typical positions at the machine are calculated as a function of time after the last discharge.

Finally, it should be stressed that ZEPHYR is not in all details a well defined experiment at present. For these calculations, therefore, choices had to be taken concerning materials and shapes of elements both for the torus and the shielding layers. Some of these choices are likely to change in the course of progressing design.

2.1 The experiment ZEPHYR

The tokamak experiment ZEPHYR will achieve ignition by heating the plasma in the pre-compression stage (cf. Fig.1) with neutral beam injectors and compressing it to the ignited state after heating. The maximum duration of "burning" in the ignited state will be about 4 seconds per discharge with an α -particle heating power of $\sim 10 - 20$ MW accompanied by a maximum neutron production rate of 4×10^{19} neutrons/sec. This maximum neutron source strength has been used for the calculations presented in this paper. Due to mechanical limitations on the cycle number for the main field coils and due to radiation damage to the coil insulator a maximum of 3000 burn-seconds

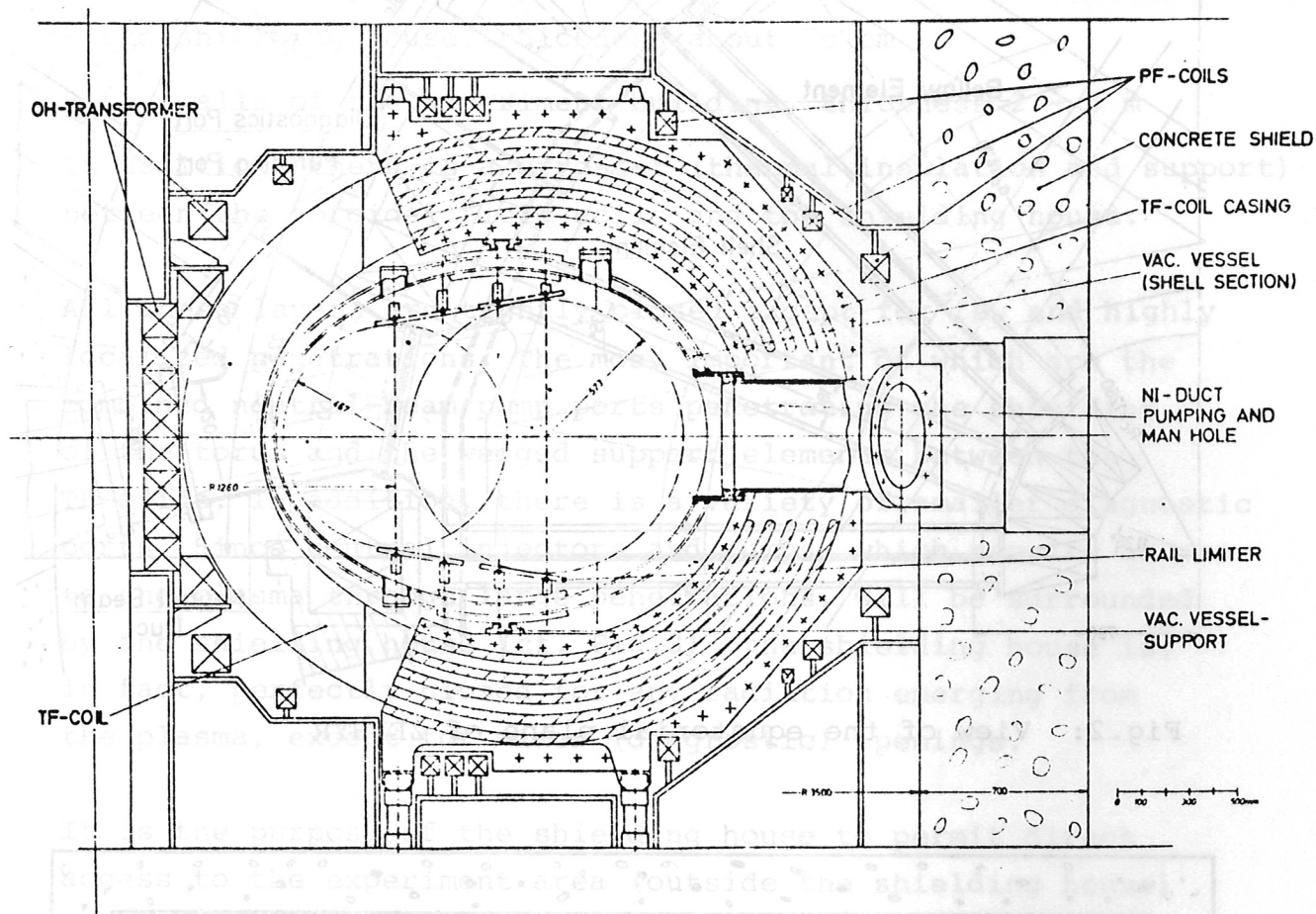


Fig.1: The lay-out of ZEPHYR

(at 4×10^{19} neutrons/sec) is envisaged for ZEPHYR. In addition, ZEPHYR will have "non-burning" modes of operation which will not contribute to the total neutron production noticeably. One of these, the mode of pure deuterium operation, is analysed in the Chapters 2.6 and 5 of this paper.

Figures 1 to 3 show some basic views of the experiment. For radiation transport purposes it is important to note that the neutron source (the plasma) is surrounded by different layers of material:

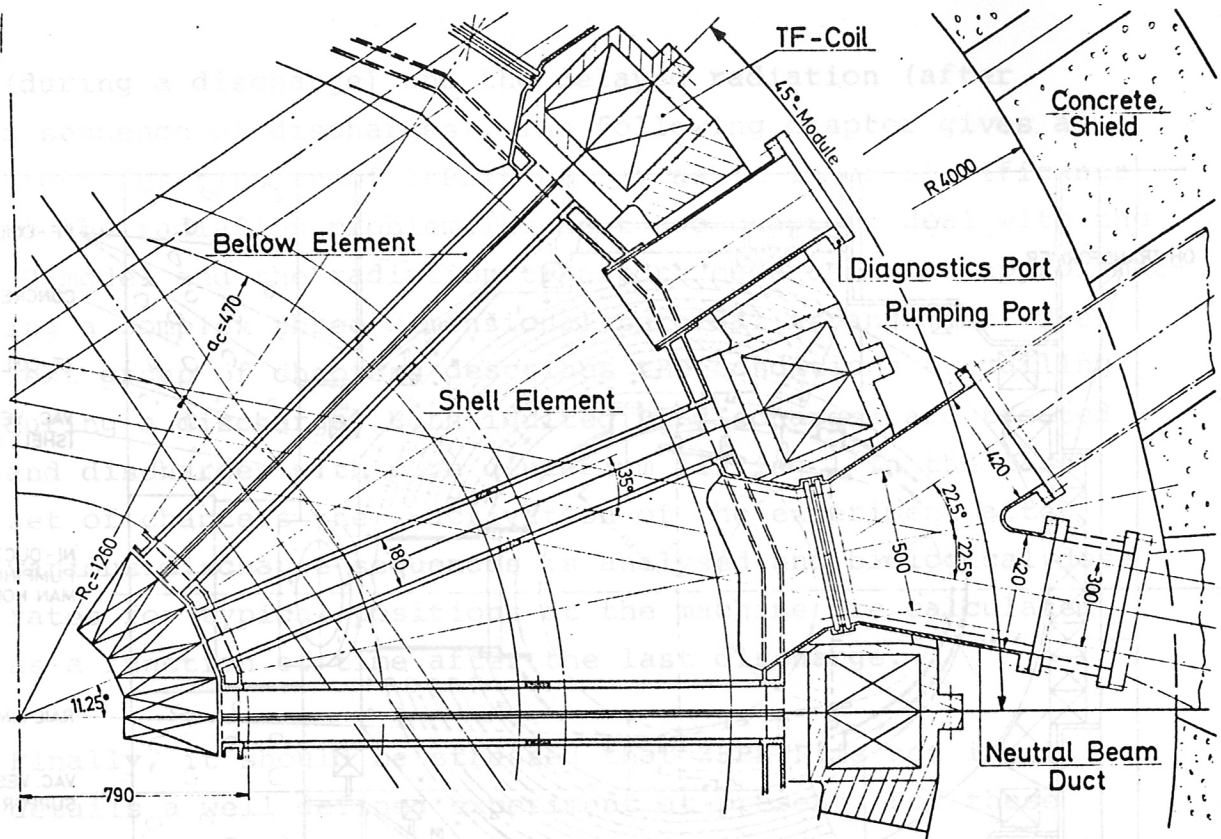


Fig.2: View of the equatorial plane of ZEPHYR

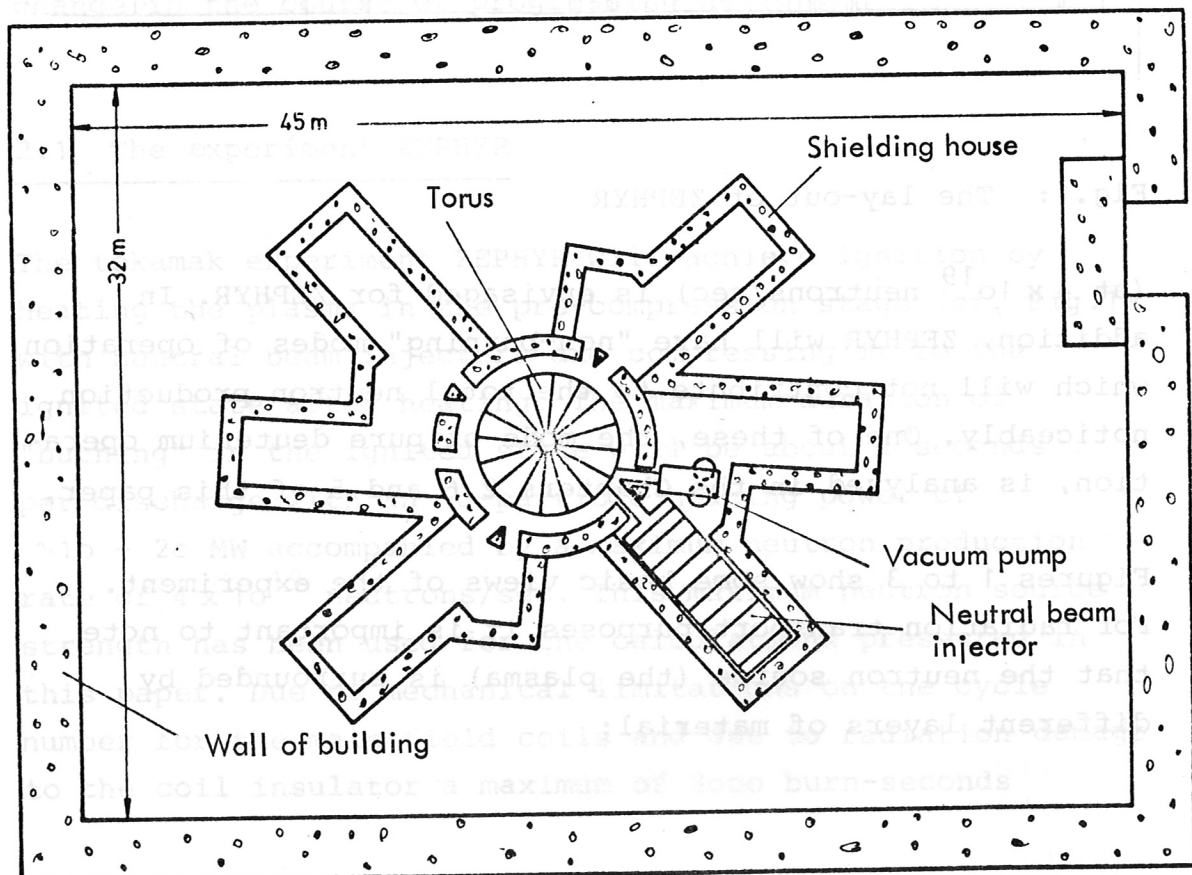


Fig.3: Building and shielding arrangements for ZEPHYR

- the vacuum vessel, average thickness 2 cm
- the toroidal field coils with wedge-shaped massive support elements in between the individual coil, 35 to 50 cm thick
- the shielding house, thickness about 70 cm
- the walls of the experiment building, thickness 2 - 3 m

In addition, there is a cryostat (thermal insulation and support) between the toroidal field coils and the shielding house.

All these layers are tightly closed except for few and highly localized penetrations. The most important of which are the combined neutral-beam/pump ports penetrating the shielding of the torus and the wedged support elements between the TF-coils. In addition, there is a variety of smaller diagnostic ports. Since neutral injectors and pumps, which require access to the plasma through large penetrations, will be surrounded by the shielding house (cf. Fig.3) the shielding house is, in fact, perfectly closed for any radiation emerging from the plasma, except for minor (diagnostic) openings.

It is the purpose of the shielding house to permit direct access to the experiment area (outside the shielding house) a few hours after a sequence of discharges. In order to reduce the radiation level during an ignited discharge to a sufficiently low level, the walls of the experiment building will be made from concrete two to three meters thick. Unlimited access is then possible outside the building. The area inside of the building cannot be entered during discharges.

2.2 The geometry of the 1D radiation transport model

The complex toroidal geometry of the experiment was transformed into a 1D-shape in particular into a set of concentric spheres (see Fig.4 and Table 1), that can be treated by a one-dimensional radiation transport code. There is a direct correspondance

between a cut through the model geometry (Fig.4) and an equatorial cut through the real experiment (Figs.2 and 3) if neutral injectors and pumps are neglected. In addition, the distinction between TF-coil-material and wedged support elements between the TF-coils at the torus outside could not be modelled. Instead the model assumes that the TF-coils fill fully the space occupied by the support wedges. This seems acceptable because both parts have similar thicknesses and are made of materials with similar radiation transport and activation properties.

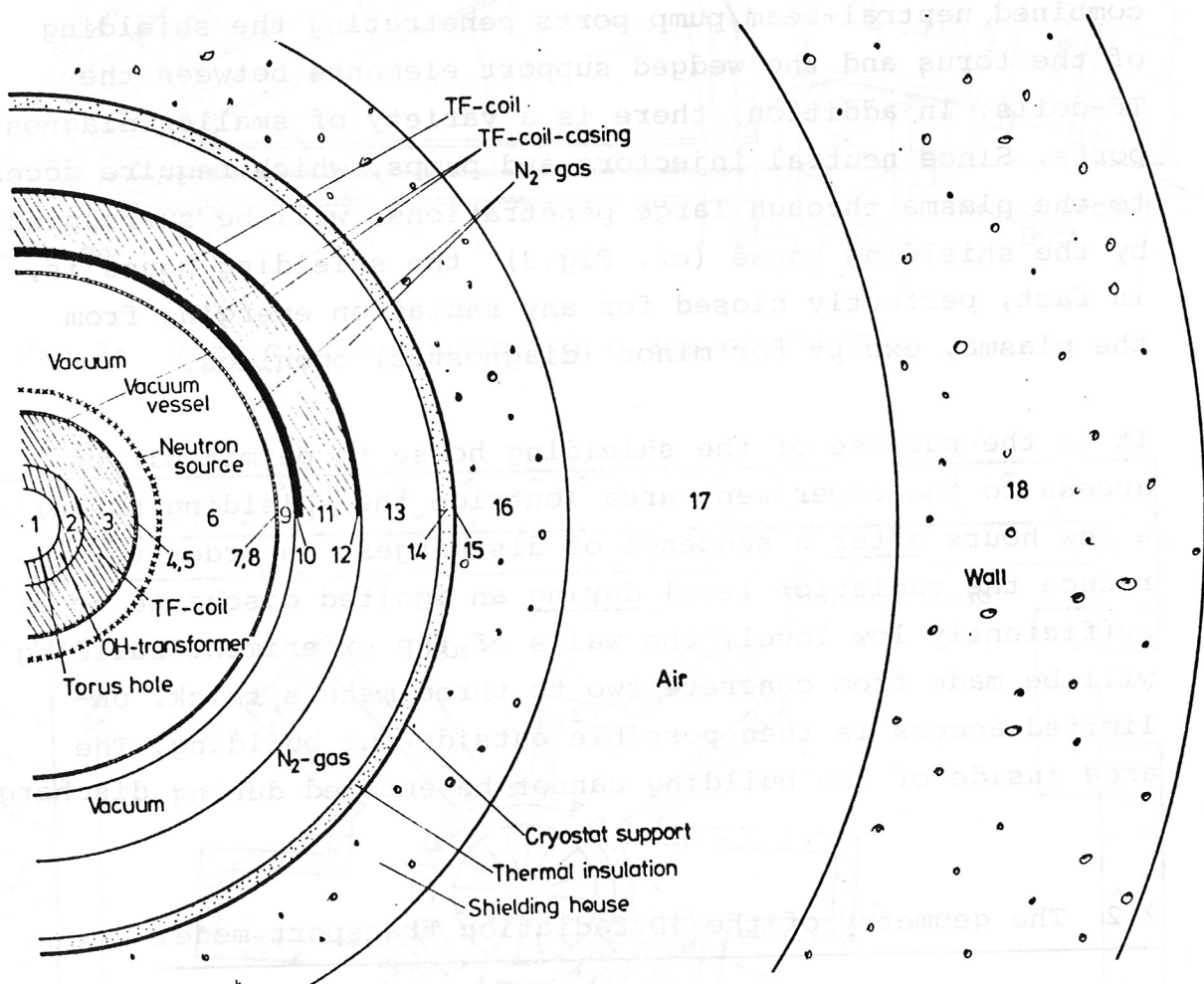


Fig.4: Shell model geometry for 1D radiation transport calculations.

Upper part: Cross section through TF-coil

Lower part: Cross section through coil-penetration

Note: Width of zone 17 (air in exp.building) not drawn to scale.

Zone nr.	Function	Material	Width	Interval nr.
1	Torus hole	Vacuum	24 cm	1
2	OH-transformer	TF-coil mixture	15 cm	2 - 7
3	TF-coil	"	33 cm	8 - 20
4	Vacuum vessel	Inconel 625	2 cm	21
5	Heat shield	Copper	0.5 cm	22
6	Vacuum	Vacuum	87.5 cm	23 - 27
7	Heat shield	Copper	0.5 cm	28
8	Vacuum vessel	Inconel 625	2 cm	29
9	Cryostat atmosphere	N ₂ -gas at 80 K	10.5 cm	30
10	TF coil casing	AISI 216 ⁺⁾	6 cm	31 - 33
11	TF coil	TF coil mixture ⁺⁾	33 cm	34 - 44
12	TF coil casing	AISI 216 ⁺⁾	4 cm	45 - 46
13	Cryostat atmosphere	N ₂ -gas at 80 K	52 cm	47 - 48
14	Thermal insulation	Styroflex foam	10 cm	49
15	Cryostat support	Aluminium alloy	3 cm	50
16	Shielding house	Borated concrete	70 cm	51 - 78
17	Air of exp. building	Air	16.47 m	79 - 87
18	Walls of exp. building	Borated concrete	2 m	88 - 127
19	Air outside exp. bldg.	Air	10 cm	128
-	Neutron source	Vacuum	0.2 cm at radius 87 cm	24

⁺⁾ Zones 10, 11, 12: material substituted by vacuum for calculation of TF-coil penetration.

Table 1: Zone and interval definitions for radiation transport calculations. Details of materials are presented in appendix A.

An attempt was made to take into account the effects of ducts in the TF-coil system. For that purpose all calculations have been performed twice. In the first case the coils are assumed unpenetrated, corresponding to the model in the upper part of Fig. 4. Results of calculations with this model are labelled "TF-coil" or "coil-shadow" throughout this paper. In the second case (lower part of Fig. 4) the outer wing of TF-coils and the coil casing are omitted (substituted by vacuum), simulating the situation along the center line of a large hole. Results for this case are labelled "coil penetration". In both cases the shielding house is modelled with its full thickness of 70 cm, since in reality it is also free of penetrations as mentioned in Chapter 2.1.

The chosen geometrical representation intends to model the radiation situation in the equatorial plane of the real experiment. Since a direct use of the equatorial major radii of the experiment for the shell model would result in some avoidable errors caused by the different geometries an effort was undertaken to compensate these by choosing appropriately adjusted radii in the model. This was done according to the following guidelines:

- Radii are adjusted such that the total 14 MeV neutron flux at the TF-coil surfaces facing the plasma is properly modelled assuming no scatter and absorption by the vacuum vessel. This flux is $2.1 \times 10^{14} \text{ n}/(\text{cm}^2 \cdot \text{sec})$ at the torus throat and $5.4 \times 10^{13} \text{ n}/(\text{cm}^2 \cdot \text{sec})$ at the outer wing of the TF-coils.
- Widths of zones filled with solid materials are kept, varied are only widths filled with gases or vacua. The position of the neutron source is varied. The total neutron source strength is kept.

This procedure results in the following radii:

	equatorial major radius in ZEPHYR	model radius
TF-coil surface, facing plasma, at torus throat	70 cm	72 cm
TF-coil surface, facing plasma, at outer torus wing	279 cm	181 cm
Plasma position (compressed)	(126 ± 47) cm	(87 ± 0.1) cm

This method will give reasonably correct fluxes for the equatorial plane in the layers adjacent to the plasma, since:

- Radiation transport through holes does not play an important role there.
- The total uncollided neutron flux is correct by way of construction of the model. Small errors may enter only since the anisotropy of the uncollided flux is somewhat geometry-dependent.
- The scattered flux (including neutron induced γ -quanta) will be rather isotropic in the vacuum vessel. Its error at the TF-coil surfaces will therefore be of the order of the ratio of TF-magnet bore surface to equivalent model surface being ~ 1.12 only.

In contrast, the fluxes in the area outside the TF-coils are strongly influenced by radiation streaming through coil penetrations, the treatment of which is rather crude in this 1D-model. Quantitatively useful data can be obtained, however, for locations sufficiently far away from the torus, where the fluxes streaming through penetrations and the fluxes passing through the coils mix. In this region a weighted average for the two model cases will be a good approximation with weights given to the two cases corresponding to the area of penetrations (7 %) and area of coils with support wedges (93 %).

2.3 Prompt radiation transport: codes and cross sections

The radiation transport calculations were performed with the one-dimensional discrete ordinates code ANISN /1/ in the P_3 , S_8 approximation⁺). The cross sections used in the calculations were taken from the coupled 100-group neutron and 21-group gamma-ray cross section library DLC-37 D /2/. Being "coupled" means that the secondary gamma-rays produced by neutron interactions appear as sources in the gamma-ray groups through the group-to-group transfer matrix. The neutron and photon-production cross sections in the DLC-37D library are weighted with a $1/E$ function for neutron energies > 0.345 eV and with a Maxwellian distribution peaked at 800 K for neutron energies ≤ 0.345 eV. Since the materials in the experiment are either at 76 K or at room temperature the utilization of these thermal cross sections may cause minor errors in the transport calculations. The photon-interaction cross sections are flat weighted.

The number of the radial meshpoints in the ANISN runs was 128. The result of the radiation transport calculations is the distribution of neutrons and prompt gamma-rays in the experimental device and the shield from which all quantities of interest can be calculated by utilization of appropriate response functions.

The kerma factors (kerma = kinetic energy released to materials) for evaluating the heat deposition rates were also taken from the DLC-37D library. For some of the elements used (N, Ca, S) Kerma factors are not provided by this library. In this case, Kerma factors of elements with neighbouring charge numbers are taken. In all solid materials inside the cryostat elements with missing kerma factors are only present as traces.

⁺) P_L indicates that the angular dependence of the group-to-group transfer cross sections are represented by a truncated Legendre polynomial expansion of order L . S_n means that the angular fluxes are evaluated at a set of n discrete directions.

2.4 Prompt radiation: energy deposition

Table 2 shows energy deposition rates for two test substances⁺, namely copper and polyethylene ((CH₂)_n), that were derived in order to provide information for the radiation load to diagnostic sensor heads. For all locations the photon contribution is quite independent of the material. In contrast, the neutron contribution strongly dominates in the case of the hydrogen-rich plastic material but is small in the metal. Since energy deposition in these materials is thus sensitive to radiation fields of different kind it is not surprising that the shielding efficiency for the outer wing of the TF-coils and for the shielding house differ for copper and polyethylene. The table gives the ratio of dose rate values inside and outside of the indicated layers:

	Cu	(CH ₂) _n
outer TF-coil wing	128	302
shielding house	424	1666

Table 3 shows energy deposition rates for that part of the TF-coil that is exposed to the maximum flux (torus throat, TF-coil side facing the plasma).

Since $1\text{W/g} = 10^3 \text{ Gy/sec} = 10^5 \text{ rad/sec}$ the accumulated dose after 3000 burn-seconds for epoxy amounts to $4.8 \times 10^9 \text{ rad}$ which is well in the range where severe radiation damage even for radiation resistant epoxies is to be expected.

Table 4 and Figs.5 and 6 provide information on the neutron and photon spectra at that location, which may be found useful for discussing radiation effects to materials.

⁺) This means probes which are small enough, not to perturb the local flux, but large enough to stop all charge particles, created inside the probe. γ -quanta produced inside the probe are assumed to leave the probe unaffected.

	Copper		Polyethylene	
	Neutrons	Photons	Neutrons	Photons
TF-coil, torus throat, plasma side (int. 2o)	0.60	2.72	24.6	2.46
Outer TF-coil wing, plasma side (int. 31)	0.38	1.59	18.5	1.44
Outer TF-coil wing, inside casing, plasma side (int. 34)	0.18	1.09	9.71	0.95
Outer surface of outer TF-coil wing, (int. 47)	1.64×10^{-3}	1.32×10^{-2}	5.57×10^{-2}	1.03×10^{-2}
Outer surface of shielding house, coil shadow (int. 79)	2.72×10^{-7}	3.46×10^{-5}	1.14×10^{-5}	2.82×10^{-5}

Table 2: Energy dose rates for copper and polyethylene probes at various locations. All values given are for center of intervals. For interval definitions see Table 1.

Material	Energy dose rate (W/g)	
	Neutrons	Photons
AISI 216	0.64	2.65
Copper	0.60	2.72
Epoxy	13.60	2.45
Epoxy/Glassfibre	5.89	2.14
TF-coil mixture	0.81	2.67

Table 3: Energy dose rates for components of TF-coil. Location is TF-coil at torus throat, plasma side (int. 2o)

	Neutron flux (n/(cm ² x sec))		Photon flux (γ/(cm ² x sec))
total flux	1.13×10^{15}	total flux	4.95×10^{14}
first group flux (13.5 - 14.9 MeV)	9.7×10^{13}	first group flux (12.0 - 14.0 MeV)	7.8×10^8
E ≥ 5 MeV	1.3×10^{14}	E ≥ 10 MeV	3.0×10^{12}
E ≥ 1 MeV	2.6×10^{14}	E ≥ 3 MeV	6.3×10^{13}
E ≥ 100 keV	7.0×10^{14}	E ≥ 1 MeV	1.6×10^{14}
thermal group flux (E < 0.414 eV)	2.4×10^{12}		

Table 4: Information on neutron and photon spectra for interval 2o (torus throat, TF-coil side facing plasma)

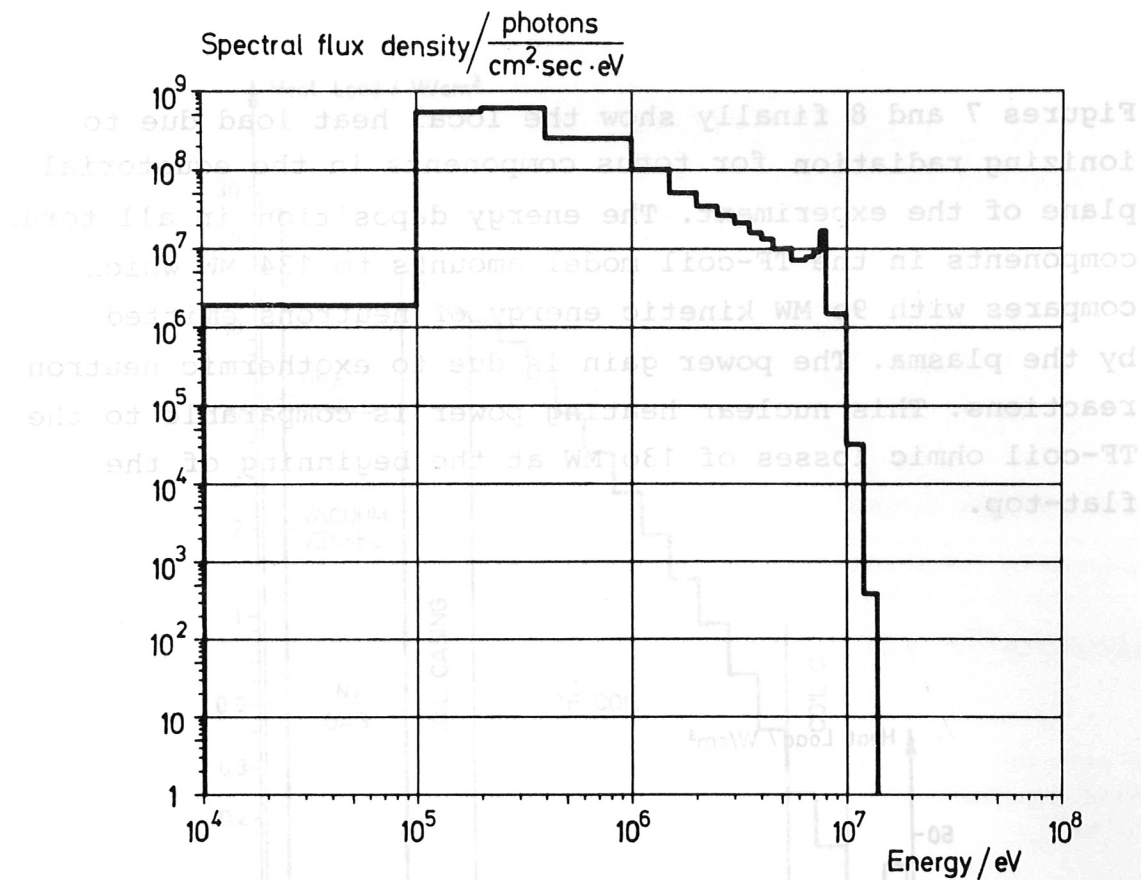


Fig.5: Photon spectrum at torus throat, vacuum side of TF-coil during DT-burn (4×10^{19} neutrons/sec)

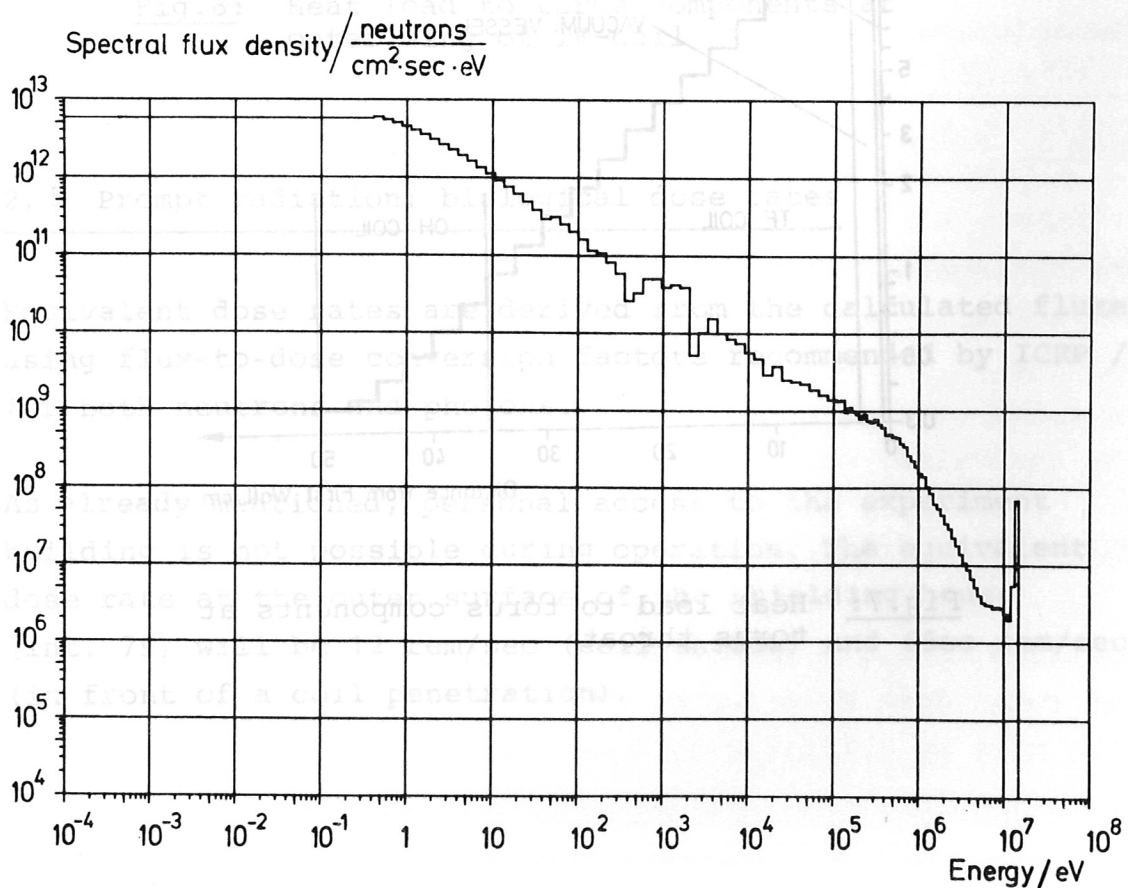


Fig.6: Neutron spectrum at torus throat, vacuum side of TF-coil during DT-burn (4×10^{19} neutrons/sec).

Figures 7 and 8 finally show the local heat load due to ionizing radiation for torus components in the equatorial plane of the experiment. The energy deposition in all torus components in the TF-coil model amounts to 134 MW which compares with 90 MW kinetic energy of neutrons emitted by the plasma. The power gain is due to exothermic neutron reactions. This nuclear heating power is comparable to the TF-coil ohmic losses of 130 MW at the beginning of the flat-top.

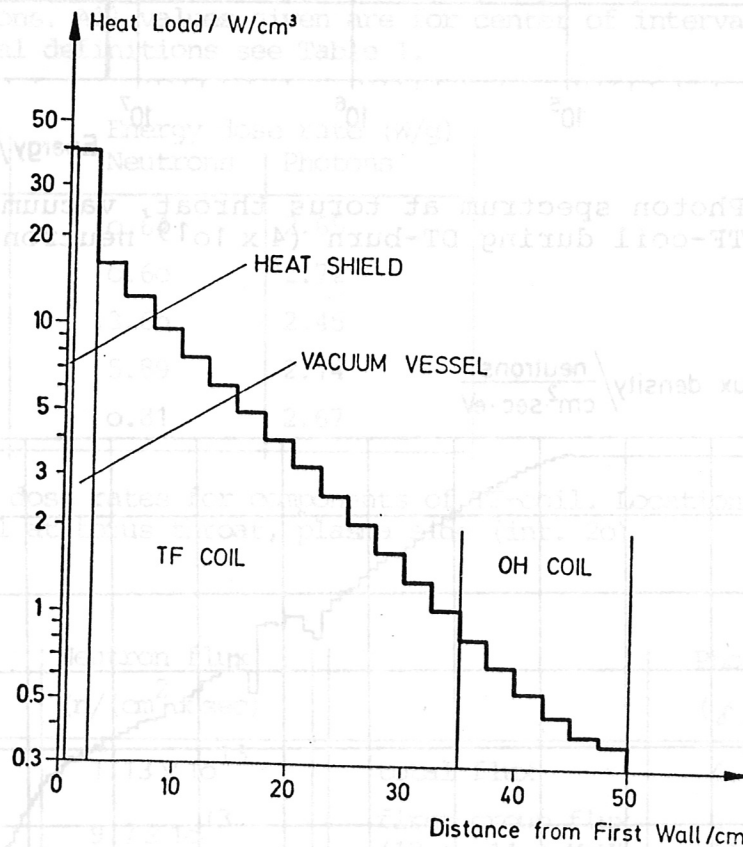


Fig.7: Heat load to torus components at torus throat

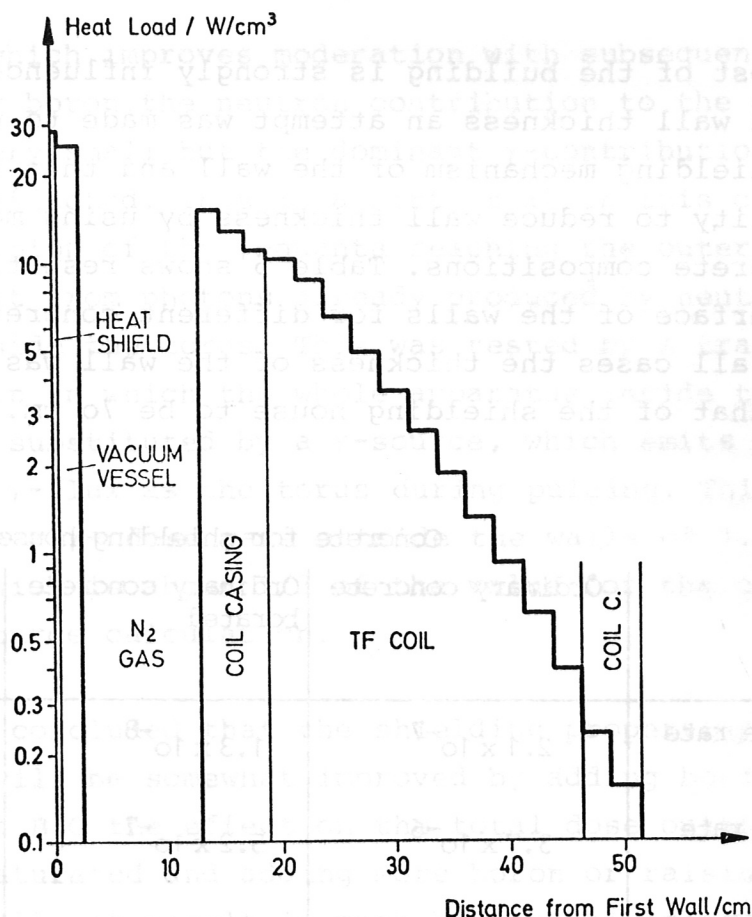


Fig.8: Heat load to torus components at outer wing of TF-coil

2.5 Prompt radiation: biological dose rates

Equivalent dose rates are derived from the calculated fluxes using flux-to-dose conversion factors recommended by ICRP /3/ for both neutrons and photons.

As already mentioned, personal access to the experiment building is not possible during operation. The equivalent dose rate at the outer surface of the shielding house (int. 79) will be 12 rem/sec (coil shadow) and 6500 rem/sec (in front of a coil penetration).

Since the cost of the building is strongly influenced by the required wall thickness an attempt was made to understand the shielding mechanism of the wall and thus to gain the possibility to reduce wall thickness by using more refined concrete compositions. Table 5 shows results for the outer surface of the walls for different concrete compositions. In all cases the thickness of the wall was assumed to be 2 m, that of the shielding house to be 70 cm.

	Concrete for shielding house and wall		
	Ordinary concrete	Ordinary concrete borated	Ordinary concrete borated hydrogen doubled
Neutron eq.dose rate (rem/sec)	2.1×10^{-7}	1.3×10^{-8}	9.8×10^{-10}
Photon eq.dose rate (rem/sec)	3.7×10^{-6}	5.2×10^{-7}	4.4×10^{-7}
Total neutron flux (n/cm ² · sec)	163.2	0.76	0.048
Thermal group n.flux (n/cm ² · sec)	162.1	0.016	0.0014

Table 5: Radiation data for outer surface of walls of building (int.128), TF-coil model.

The table shows that in ordinary concrete neutrons are moderated but not effectively captured, and the resulting flux at the outside of the wall consists of more than 99 % thermal neutrons. In spite of that high neutron flux, the photon contribution to the equivalent dose rate dominates by a factor ~20. These photons are produced by neutron capture inside the concrete wall, since reducing the neutron flux by adding boron to the concrete reduces the photon equivalent dose rate, too (center column). This addition of 0.5 % (by volume) of B₄C to the concrete reduces the total dose by a factor of 7. If the neutron flux is reduced even more by artificially doubling the hydrogen content of the

concrete which improves moderation with subsequent neutron capture by boron, the neutron contribution to the dose rate becomes very small but the dominant γ -contribution stays nearly unaffected. This is a hint, that in this case a large fraction of the γ -quanta reaching the outer side of the wall result from photons already produced by neutron interaction inside the torus. This was tested by a transport calculation in which the whole apparatus inside the shielding house was substituted by a γ -source, which emits the same spectral γ -flux as the torus during pulsing. This results in a γ -dose rate outside the walls of 1.6×10^{-7} rem/sec which is about 1/3 of the value for the corresponding neutron-source calculation.

It can be concluded that the shielding properties of ordinary concrete will be somewhat improved by adding boron. At 0.5 % (by volume) of B_4C the effect on the total dose outside the walls is already saturated and adding more boron or raising the hydrogen content will not result in much better shielding properties.

Outside the building walls the radiation penetrating through holes in the TF-coils will be smeared out and the procedure of the weighted average for TF-coil model and TF-penetration model, as indicated in chapter 2.2 will give a reasonable approximation. Assuming, that the possible 3000 burn-seconds are consumed in one year, the accumulated prompt dose outside the walls amounts to:

78 mrem	(ordinary concrete)
11 mrem	(borated concrete).

This is close to the permissible dose for the general population of 30 mrem. Therefore, the wall thickness has to be increased in order to reduce the yearly dose well below the legal limit.

2.6 Prompt biological dose rates for deuterium operation

Prior to investigating ignited deuterium/tritium discharges in ZEPHYR a period of various deuterium and hydrogen discharges will precede. The resulting plasmas are not "ignited" but may produce copious neutrons. In particular, the pure deuterium mode of operation (neutral beams of D-atoms heat a deuterium plasma, which is compressed and kept in the compressed state until natural cooling occurs) will produce about 1×10^{17} neutrons/puls at 2.5 MeV accompanied by 3.5 % of parasitic 14.1 MeV neutrons. Assuming 5000 pulses in 1 year the weighted average of the two model case for the equivalent dose rate outside the building (borated concrete assumed) will be 1.2×10^{-5} rem/a. This is only some 3 orders of magnitude less than for 1 year of ignited discharges allowing a reduction of the shielding thickness by only about 90 cm.

3.1 Delayed gamma-ray transport: codes and cross sections

For determining the activation of the machine and the resulting activation gamma-ray sources in the different components of the experiment a computer code called GSOURC was written. By this code, the neutron fluxes as calculated for the prompt radiation problems are multiplied with the activation cross sections for all relevant activation reactions of the materials present in the apparatus. Taking into account the radioactive decay of the parent nuclides produced and the subsequent build-up and decay of daughter and grand-daughter nuclides the space- and time-dependent activity of the machine is determined for given sequences of pulses. By utilization of the energies and intensities of the gamma-rays emitted by the different radionuclides the activation rates are then processed into space-, energy-, and time-dependent gamma-ray sources which are input to new ANISN transport calculations for the delayed gamma-rays. A list of the activation reactions and decay chains considered is given in Appendix B. For the present treatment, only those activation reactions were taken into account which lead to gamma-ray emitting nuclei.

The activation cross sections used were taken from the DLC-33/Montage library which was modified by adding some activation reactions and by regarding the reactions which lead to isomeric states. The half-lives of the radionuclei, the energies of the gamma-rays emitted, and their respective percentage yields per disintegration were taken from a Jülich compilation of gammalines /4/.

The delayed gamma-ray transport calculations were performed for 11 gamma-ray groups whose energy boundaries are given in Table 6. The gamma-ray interaction cross sections were generated with the SMUG module of the AMPX system /5/ using ENDF data.

Group	γ -energy range (MeV)
1	5 - 3
2	3 - 2.5
3	2.5 - 2
4	2 - 1.5
5	1.5 - 1
6	1 - 0.7
7	0.7 - 0.4
8	0.4 - 0.2
9	0.2 - 0.1
10	0.1 - 0.05
11	0.05 - 0.01

Table 6: γ -energy group structure for delayed radiation transport calculations

The ANISN runs are performed separately for the two model cases (TF-coil and coil penetration), for several activation sequences and for each of these cases for about 14 different times after shutdown called "cooling times". Biological dose rates are determined from the calculated γ -fluxes, again, by using ICRP flux-to-dose coefficients /3/.

3.2 Activation after final shutdown

To determine activation data for the period following shutdown of the experiment, it is required to define the neutron production rate for the time preceding. It was assumed that the duty-cycle⁺⁾ of the experiment grows as the square of the DT-operation time, lasting 4 years. During that time neutron production corresponds to 3000 seconds of plasma-burn

^{+) For that purpose duty-cycle is defined in terms of neutron production N in an interval of operation time Δt :}

$$DC = \frac{N}{\Delta t \times 4. \times 10^{19} \text{ n/sec}},$$

being roughly the number of burn-seconds per week

(4×10^{19} neutrons/burn-sec), discretized into 750 discharges of 4 sec duration. This results in a sequence of pulses with gradually narrowing intervals between discharges, the last and shortest of which lasts 15.4 h. 11 discharges are carried out during the first year, 82 during the second year, 225 during the third and 432 during the last year.

The most important building materials of the apparatus are stainless steel, copper, Inconel for the vacuum vessel and (borated) concrete. Figure 9 shows the specific γ -source strengths for layers of these materials adjacent to the outer wing of the vacuum vessel and for concrete at the outer surface of the shielding house. In the cooling time interval 1 d to ~ 100 d, which is most essential in view of maintenance

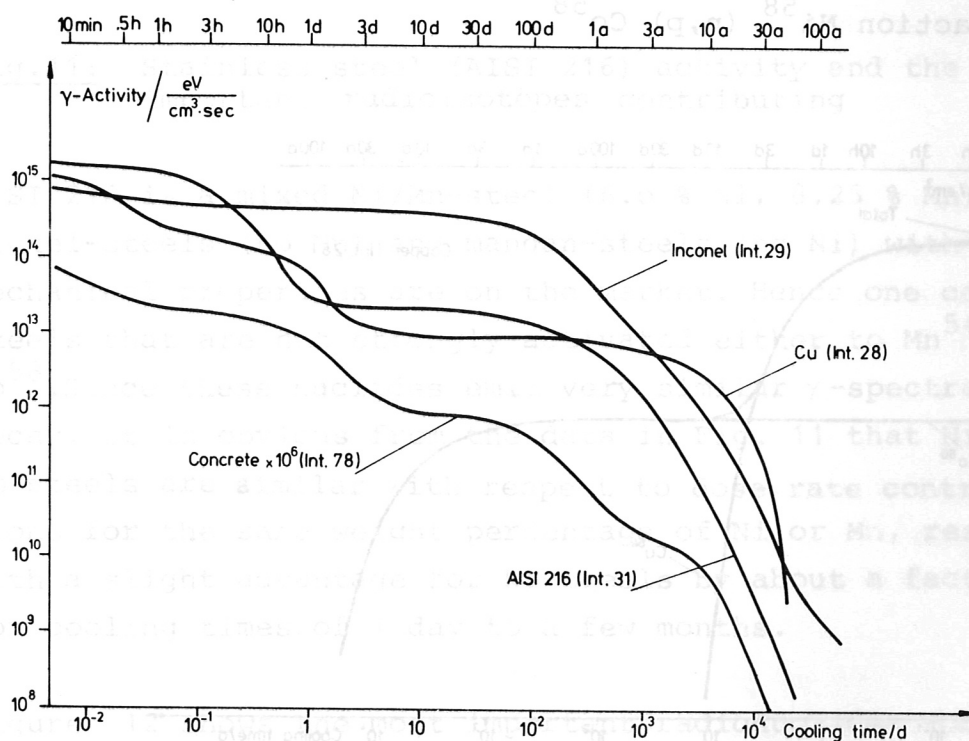


Fig.9: Specific γ -source strengths for various materials expressed as power released in the form of γ -quanta. Inconel, copper and AISI 216 are exposed to very similar neutron fluxes. The concrete data are given for the outermost interval of the shielding house. All curves are calculated using the TF-coil model.

and repair, the specific γ -activity of Inconel is more than about one order of magnitude larger than for AISI 216 or for copper. As will be shown the vacuum vessel therefore contributes dominantly to biological dose-rates.

In Figs. 10 to 13 the activity^{+) of these materials is analysed more in detail for the TF-coil model. Copper (Fig.10) is transmuted into Cu^{64} (half-life 12.8 h) and into Co^{60} (half-life 5.3 a). After a few days of cooling the activity remains on the rather low level of 10^{-4} Ci/cm³. Figure 11 shows the activation of AISI 216 which for cooling times from 1 d to a few years is dominated by Cr^{51} , Mn^{54} and Co^{58} . Cr^{51} (half-life 27.8 d) contributes only insignificantly to dose rates since it emits a weak (320 keV) γ -quantum in only 10 % of its decays. Mn^{54} (half-life 316 d) is produced predominantly by the Mn^{55} (n, 2n) Mn^{54} reaction and Co^{58} (half-life 71.3 d) by the reaction Ni^{58} (n,p) Co^{58} .}

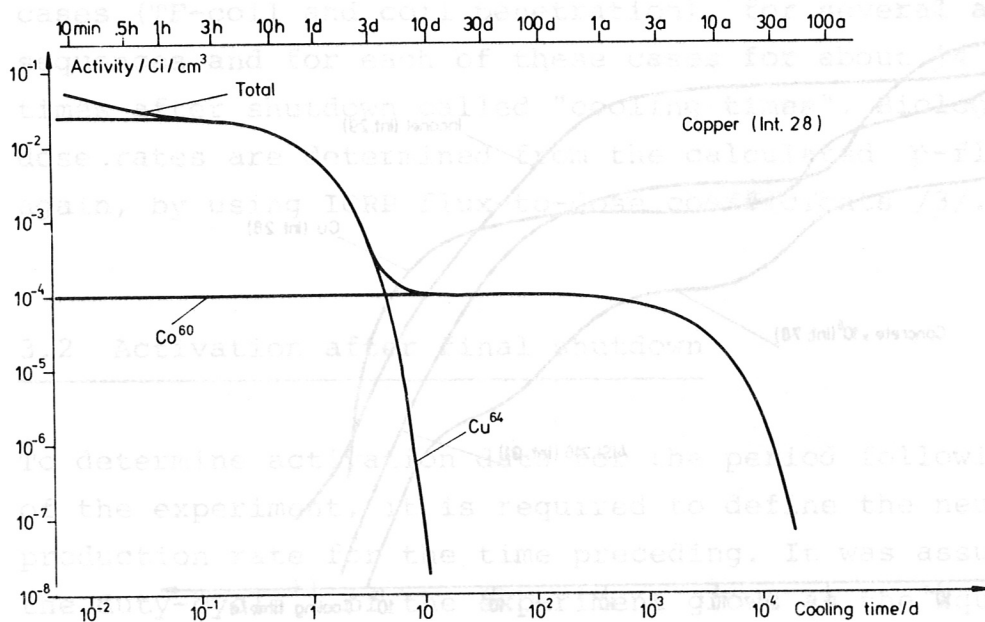


Fig.10: Copper activity and the most important radioisotopes contributing. (Note: $1\text{Ci} = 3.7 \times 10^{10}$ decays/sec)

^{+) This analysis is restricted to radioisotopes emitting γ -quanta}

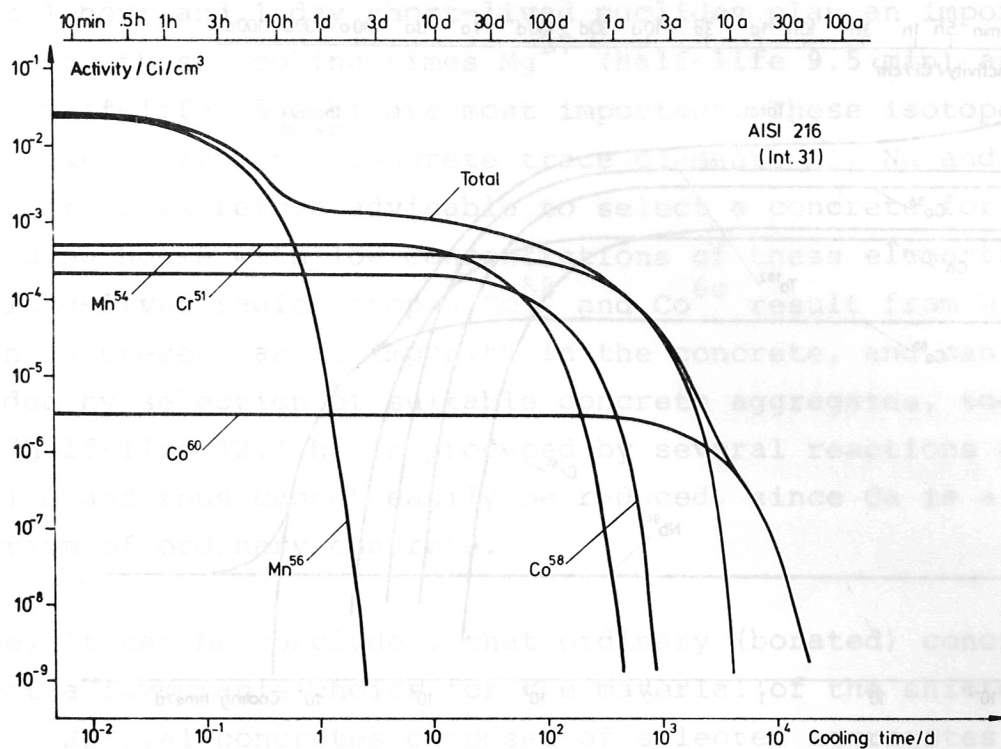


Fig.11: Stainless steel (AISI 216) activity and the most important radioisotopes contributing

AISI 216 is a mixed Ni/Mn-steel (6.0 % Ni, 8.25 % Mn). Nickel-steels (no Mn) and mangan-steels (no Ni) with similar mechanical properties are on the market. Hence one can choose steels that are not strongly activated either to Mn^{54} or to Co^{58} . Since these nuclides emit very similar γ -spectra during decay, it is obvious from the data in Fig. 11 that Ni- or Mn-steels are similar with respect to dose-rate contributions for the same weight percentage of Ni or Mn, respectively, with a slight advantage for Ni-steels by about a factor of 2 for cooling times of 1 day to a few months.

Figure 12 shows the most important radionuclides for the Ni-based alloy Inconel 625. In the cooling time interval of 1 day to a few hundred days the activity is dominated by Ta^{182} (half-life 115 d) from the reaction $Ta^{181} (n, \gamma) Ta^{182}$ and from Co^{58} (half-life 71.3 d) produced predominantly by

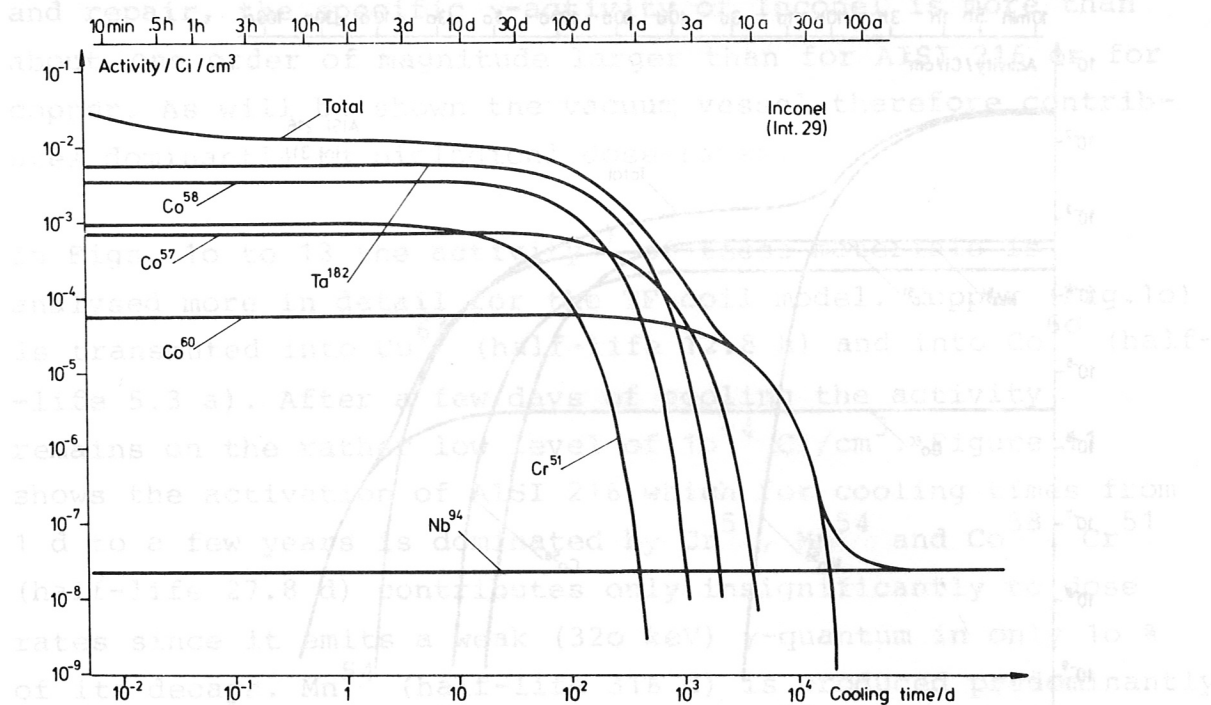


Fig.12: Inconel 625 activity and the most important radioisotopes contributing

the Ni^{58} (n,p)-reaction. Since the Ta-content of Inconel is a poorly defined quantity⁺) it might be possible to select batches of Inconel with low Ta-content. Assuming a tantalum-free Inconel alloy the possible gain, however, is only about a factor of 2 due to the presence Co^{58} , Co^{60} stemming from Ni. After a few years of cooling Co^{60} (half-life 5.3 a) remains the dominant source of γ -quanta until after about 100 years only Nb^{94} (half-life 20.000 a) from the Nb^{93} (n, γ)-reaction remains, although on a very low level (18 mCi for the entire apparatus).

Finally, in Fig.13 the activity of borated ordinary concrete is analysed for the outermost interval of the shielding house. As will be shown in the next chapter the dose rates in the experiment building are dominated by the activity of the shielding house concrete. Since access to the building is required already after cooling times of between

⁺) Information on Ta-content was available only in the form $\text{Ta}+\text{Nb}=3.7\%$. For these calculation half of this weight percentage was attributed to each single element.

about 1 hour and 1 day short-lived nuclides play an important role. For these cooling times Mg^{27} (half-life 9.5 min) and Na^{24} (half-life 15.0 h) are most important. These isotopes are produced from the concrete trace elements Al, Na and Mg, only. It is therefore advisable to select a concrete for the shielding house with low concentrations of these elements. The long-lived radioisotopes Co^{58} and Co^{60} result from Ni, which is present as an impurity in the concrete, and can be avoided by selection of suitable concrete aggregates, too. K^{42} (half-life 12.4 h) is produced by several reactions of calcium and thus cannot easily be reduced, since Ca is a main fraction of ordinary concrete.

Hence, it can be concluded, that ordinary (borated) concrete is not a favourable choice for the material of the shielding house. Special concretes composed of selected aggregates will result in considerably better shielding properties.

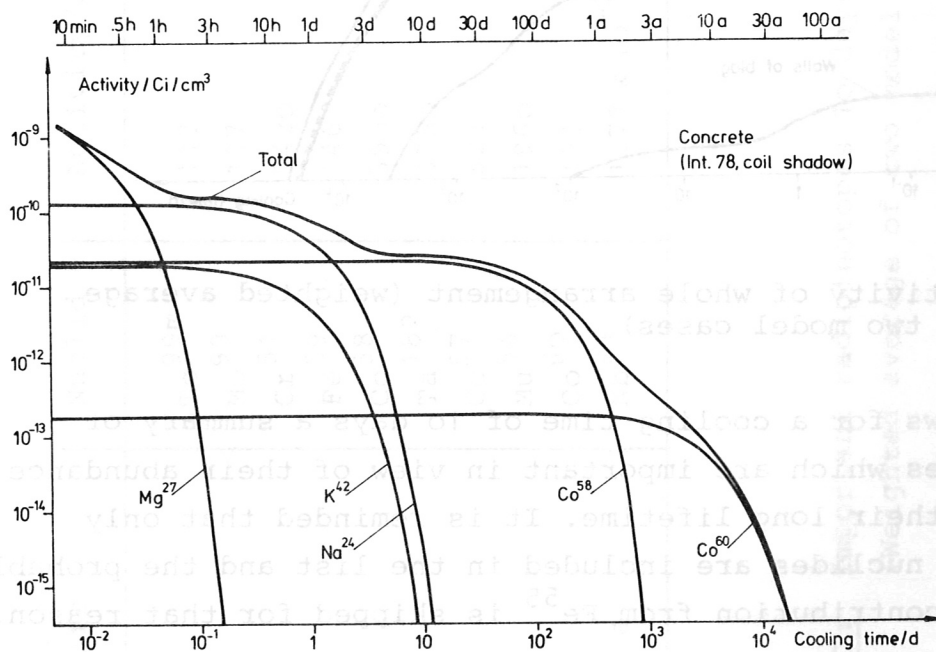


Fig.13: Concrete activity and the most important radioisotopes contributing.

Figure 14 shows the activity (including only γ -ray emitting radioisotopes) of the whole assembly as a function of cooling time. As one can see the dominant sources are the vacuum vessel and the OH-trafo with TF-coils and casing. The shielding house and the building contribute orders of magnitude less than the torus itself.

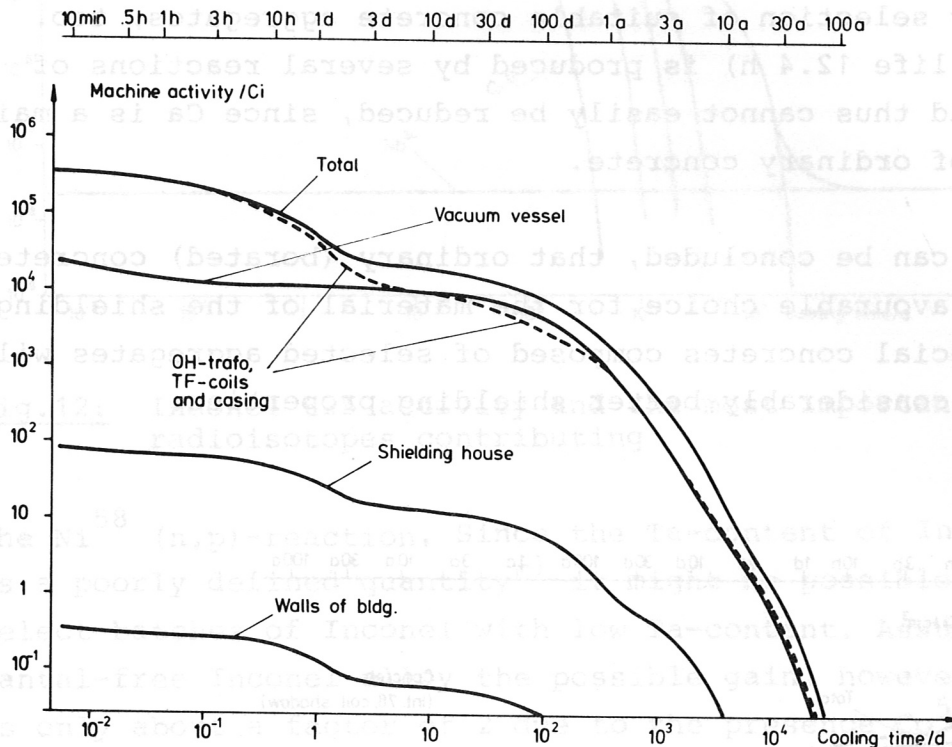


Fig.14: Activity of whole arrangement (weighted average of two model cases)

Table 7 shows for a cooling time of 10 days a summary of radioisotopes which are important in view of their abundance as well as their long lifetime. It is reminded that only γ -emitting nuclides are included in the list and the probably very large contribution from Fe^{55} is skipped for that reason.

Half-life	Nuclid	Activity/Ci	Remarks
6.02 h	Tc ^{99m}	113	Tc ^{99m} is the result of Mo ⁹⁹ -decay
66.2 h	Mo ⁹⁹	117	From Inconel and AISI 216 only
27.8 d	Cr ⁵¹	5420	From Inconel, AISI 216 (and concrete)
44.6 d	Fe ⁵⁹	146	" " " " (" ")
71.3 d	Co ⁵⁸	3900	" " " " (" ")
115 d	Ta ¹⁸²	4750	From Inconel only
270 d	Co ⁵⁷	824	From Inconel, AISI 216 (and concrete)
313 d	Mu ⁵⁴	1960	" " " " (" ")
5.3 a	Co ⁶⁰	164	From TF-coils and vacuum vessel predominantly
20.000 a	Nb ⁹⁴	1.77 x 10 ⁻²	From Inconel (and AISI 216)

Table 7: Important radioisotopes 10 days after last discharge
(Weighted average of two model cases)

3.3 Delayed radiation: biological dose rates

Resulting from the γ -sources described in the previous chapter a photon field is established in the arrangement, the most important response function of which, namely the equivalent dose rate, will be given for some typical locations.

Figure 15 shows the equivalent dose rate for the center of the vacuum vessel. There is little difference between the two model cases for that location. The dose rate curves do not drop steeply until after about 100 days the dominant Inconel activities start to decay. For cooling times of 1 day to about 100 days the dose-rates amount to more than about 10^3 rem/h which excludes personal access to the vacuum vessel. A restricted access becomes possible, again, after about 20 years of cooling at a level of 1 rem/h.

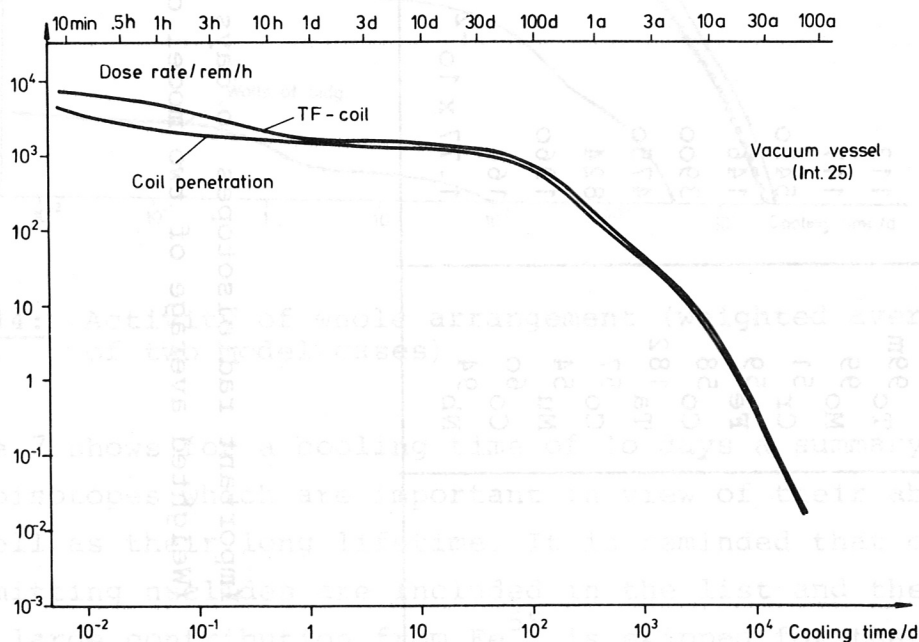


Fig.15: Equivalent dose rate inside the vacuum vessel

Figure 16 shows dose rates near the outer surface of the outer wing of the TF-coils, inside the shielding house. As expected, the two model cases differ considerably. This shows that dose rates outside the TF-coils will strongly depend on the location. In front of a TF-coil penetration they will be two to three orders of magnitude higher than in the coil shadow. According to these calculations access is possible, in principle, to a workplace in the TF-coil shadow after a few days of waiting at a level of 0.1 rem/h. In practice, however, it is likely that radiation from near-by penetrations will be scattered into the coil-shadow region and will thus rise the local dose rates to prohibitive values. It is beyond the possibilities of these 1 D-calculations to consider such effects quantitatively.

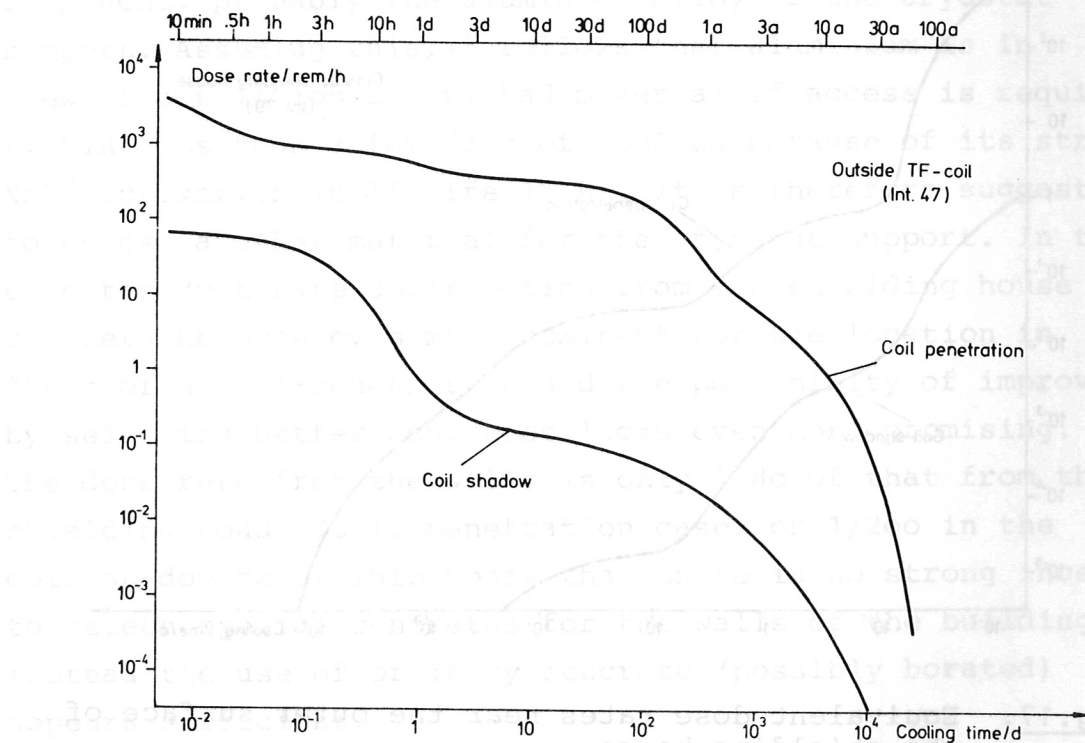


Fig.16: Equivalent dose rates near the outer surface of the TF-coils.

Figure 17 shows dose rates outside the shielding house. Again the two model cases differ considerably. Using the results from the coil-penetration model as a worst-case estimate for a workplace in front of a TF-coil-penetration, access is possible after about 3 hours of cooling at less than 1 rem/h. This is too high, however, for routine access⁺). As will be shown, this dose rate results primarily from the activation of the shielding concrete used. Since there are suggestions (cf. Chapter 3.2) for reducing the concrete activity it appears possible to reduce this dose-rate considerably without increasing the shielding house thickness.

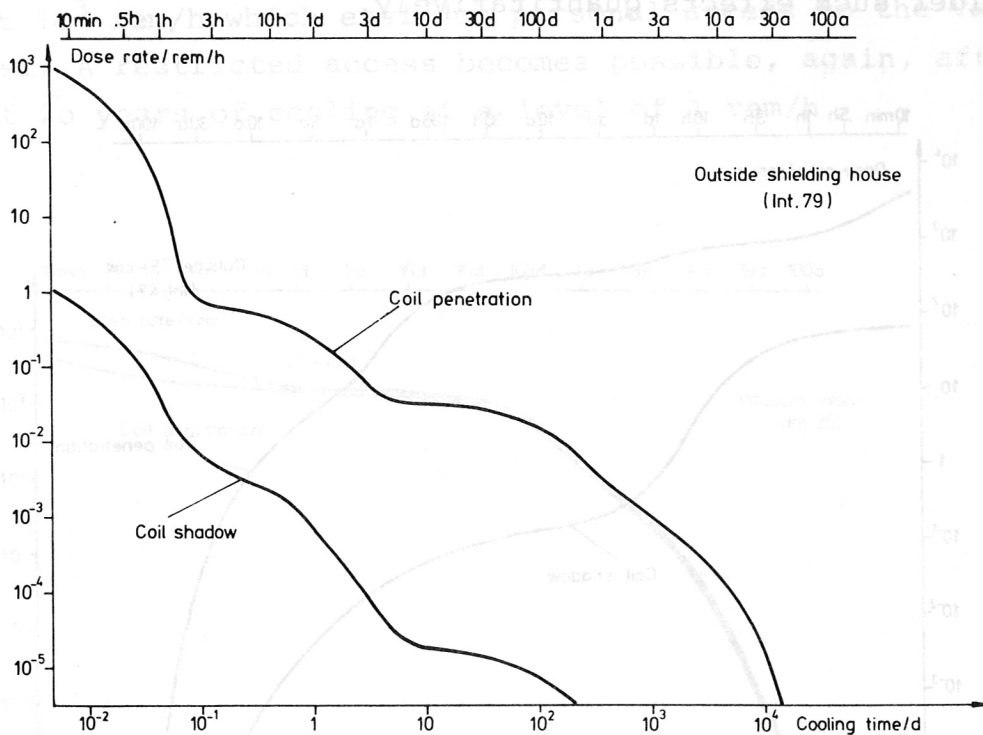


Fig.17: Equivalent dose rates near the outer surface of the shielding house.

⁺) By German law, radiation workers are allowed to receive up to 5 rem in one calendar-year, but not more than 2.5 rem in any quarter calendar-year (whole body radiation).

For a cooling time typical for access to the experiment building (10 hours) and a cooling time typical for access to the interior of the shielding house (10 days) dose rate contributions from various components of the assembly are determined by "switching off" all other delayed γ -sources in the ANISN radiation transport calculations.

Table 8 shows the result for 10 h cooling time. Outside the shielding house in the coil-shadow the shielding house itself contributes 62 % to the dose rate, the remainder mostly due to the TF-coils with their casing. More important because of the absolute higher dose rates is the result for the coil penetration. Here 74 % of the dose rate is due to the shielding house concrete, the rest stems predominantly from the vacuum vessel (5 %) and an unidentified other component, probably the aluminium alloy of the cryostat support. Assuming this, it follows that aluminium is in view of activation a very bad material if access is required within less than a few days of cooling because of its strong Na^{24} activation (half-life 15 h). It is therefore suggested to choose another material for the cryostat support. In this case the dose rate contribution from the shielding house concrete becomes even more dominant for the location in front of a coil-penetration and the possibility of improvement by selecting better concretes looks even more promising. The dose rate from the walls is only 1/80 of that from the shielding house (coil-penetration case) or 1/200 in the coil shadow case. This means that there is no strong incentive to select special concretes for the walls of the building, instead the use of ordinary concrete (possibly borated) appears sufficient.

Table 9 gives dose rate contributions for 10 days cooling time. Inside the vacuum vessel the dose rate is strongly dominated (97 %) by the Inconel of the vacuum vessel, followed

to from		Inside vacuum vessel TF-coil model (int. 25)	Outside TF-coil coil shadow (int. 47)	Outside TF-coil in front of coil penetration (int. 47)	Outside shielding house coil shadow (int. 79)	Outside shielding house in front of coil penetration (int. 79)
Full assembly		$1.95 \cdot 10^3$	4.95	$6.90 \cdot 10^2$	$1.81 \cdot 10^{-3}$	0.431
Vacuum vessel (Inconel pieces only)		$1.51 \cdot 10^3$	$6.25 \cdot 10^{-5}$	$3.75 \cdot 10^2$	$2.34 \cdot 10^{-9}$	$2.18 \cdot 10^{-2}$
Shielding house		1.09	0.275	38.5	$1.13 \cdot 10^{-3}$	0.321
TF-coils + casing		$2.64 \cdot 10^2$	4.39	1.34	$5.84 \cdot 10^{-4}$	$2.51 \cdot 10^{-4}$
Walls of exp. building		$2.82 \cdot 10^{-7}$	$4.44 \cdot 10^{-9}$	$4.04 \cdot 10^{-6}$	$5.61 \cdot 10^{-6}$	$3.85 \cdot 10^{-3}$

Table 8: Dose rates (rem/h) at various locations and dose-rate contributions from different components after 4 years, 3000 burn-sec.DT-operation and 10 hours cooling time

to from	Inside vacuum vessel TF-coil model (int. 25)	Outside TF-coil coil shadow (int. 47)	Outside TF-coil in front of coil penetration (int. 47)	Outside shielding house coil shadow (int. 79)	Outside shielding house in front of coil penetration (int. 79)
Full assembly	$1.39 \cdot 10^3$	0.140	$3.38 \cdot 10^2$	$1.76 \cdot 10^{-5}$	$3.01 \cdot 10^{-2}$
Vacuum vessel (Inconel pieces only)	$1.35 \cdot 10^3$	$4.10 \cdot 10^{-6}$	$3.34 \cdot 10^2$	$1.29 \cdot 10^{-9}$	$1.89 \cdot 10^{-2}$
Shielding house	$3.52 \cdot 10^{-2}$	$2.42 \cdot 10^{-3}$	1.84	$1.49 \cdot 10^{-5}$	$1.09 \cdot 10^{-2}$
TF-coils + casing	33.3	0.138	0.274	$2.42 \cdot 10^{-6}$	$8.90 \cdot 10^{-6}$
Walls of exp. building	$2.35 \cdot 10^{-10}$	$6.04 \cdot 10^{-12}$	$6.17 \cdot 10^{-9}$	$3.03 \cdot 10^{-7}$	$2.32 \cdot 10^{-4}$

Table 9: Dose rates (rem/h) at various locations and dose-rate contributions from different components after 4 years, 3000 burn-sec. DT-operation and 10 days cooling time.

by the dose rates from the TF-coils with casing (2.4 %). Assuming that the vacuum vessel is made from stainless steel instead of Inconel the possible reduction of dose rate from the vacuum vessel can be estimated from the data given in Fig.9. It amounts to nearly a factor of 20. But this gain is not enough to make personal access to the vacuum vessel possible.

Outside the TF-coils, in the coil shadow, the contribution from the TF-coils and their casing dominates (98.5 %). In front of a penetration the radiation from the vacuum vessel plays the most important role (99 %).

Outside the shielding house results are similar to the 10 h cooling time case. The data show that the activity of concrete decays away faster than that of Inconel and AISI 216 steel. In addition, the Na^{24} activity of the aluminium alloy for the cryostat support has vanished due to its short half-life of 15 hours.

4. Delayed radiation after 10 days of DT-pulsing

In order to investigate the effects of a short activation sequence, a situation at the beginning of the DT-burning period was simulated. Since it appears likely that long burning pulses cannot be achieved until after a long learning phase it was assumed that one puls of 0.4 burn-seconds is achieved at each one of 10 consecutive days. The data given does not take into account a possible activation due to a prior machine operation with deuterium.

Figure 18 gives the resulting biological dose rate inside the vacuum vessel. Generally, these curves slope down steeper than the corresponding curves after a long operating period (cf. Fig.15) since activities with half-lives less than about 10 days have already reached saturation whereas activities with longer half-lives have not yet achieved a strong build-up. After a cooling time of 3 days to about 100 days the dose rate amounts to some 10 rem/h. It is thus impossible to enter the vacuum vessel after a neutron production which is equivalent to one full burning discharge of 4 burn-seconds.

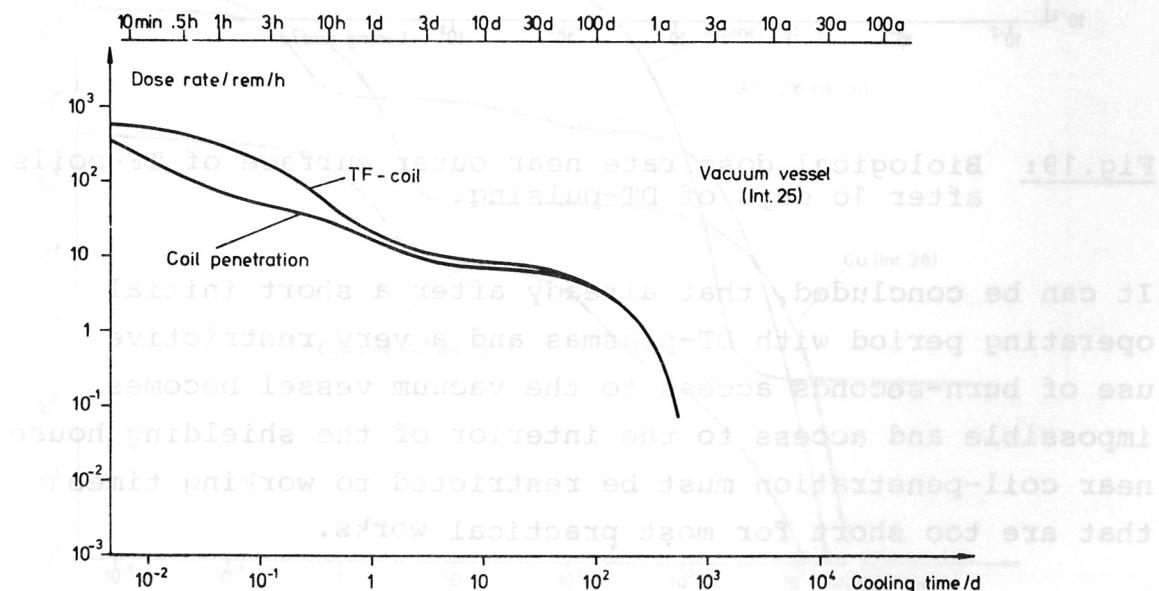


Fig. 18: Biological dose rate inside the vacuum vessel after 10 days of DT-pulsing

Figure 19 gives equivalent dose rates for the outer surface of the TF-coils. For a cooling time of about 10 days access to a position in front of a coil penetration is possible only for less than about 1 hour per quarter-year, access to a workplace in the coil shadow appears possible for useful working times, even if the effect of stray radiation from near-by penetrations is taken into account.

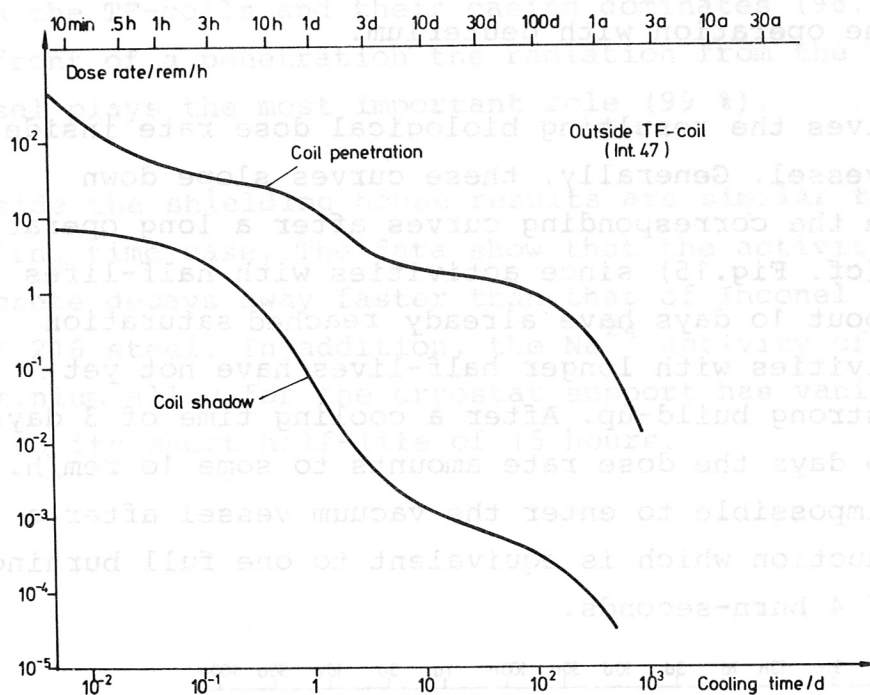


Fig.19: Biological dose rate near outer surface of TF-coils after 10 days of DT-pulsing.

It can be concluded, that already after a short initial operating period with DT-plasmas and a very restrictive use of burn-seconds access to the vacuum vessel becomes impossible and access to the interior of the shielding house near coil-penetration must be restricted to working times that are too short for most practical works.

5. Delayed radiation after one year of deuterium pulsing

It was assumed that 2000 discharges of the pure deuterium operating mode defined in Chapter 2.7 (deuterium beams heating a deuterium plasma with subsequent plasma compression) are equally distributed over one year. Plasma simulation calculations show, that this discharge sequence is equivalent in view of neutron production to about 12.000 discharges in one year of a mode with deuterium beams heating a hydrogen plasma, the resulting DH-plasma being compressed and kept in the compressed state until cooling occurs. The following values are thus valid for both these pulsing scenarios. In the second case (12.000 discharges) the validity is restricted to cooling times longer than the assumed interval between consecutive pulses (4.4 hours).

Figure 2o gives the resulting delayed γ -source strengths. Since the curves of Inconel, AISI 216, and copper are for

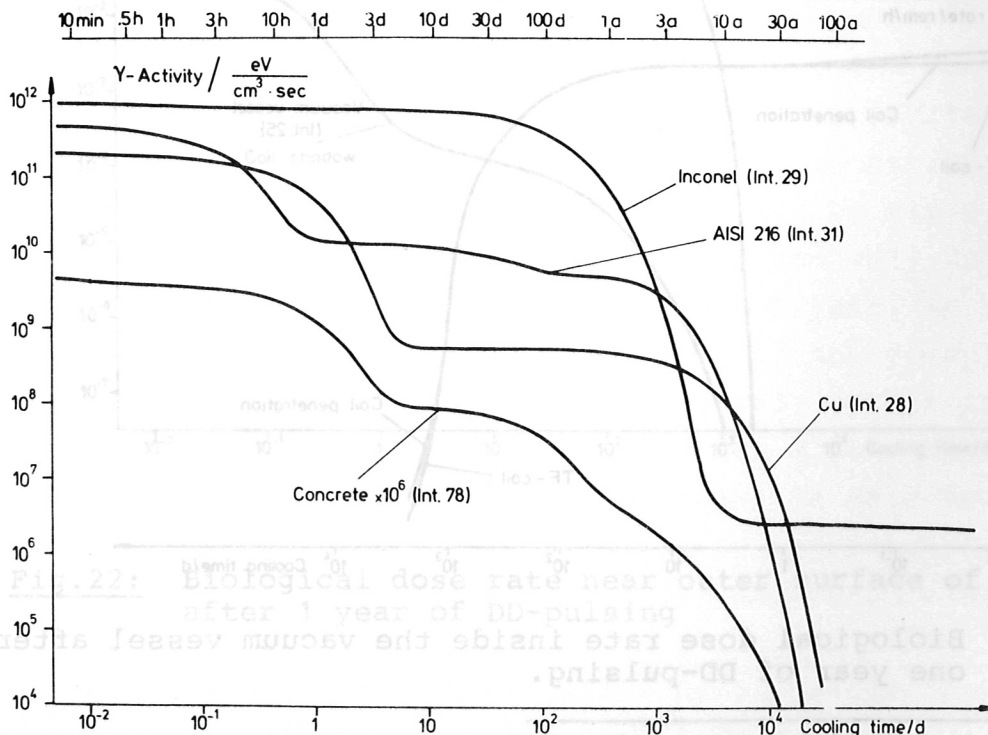


Fig. 2o: Specific γ -source strengths for various materials expressed as power released in the form of γ -quanta. Inconel, copper, and AISI 216 are exposed to very similar neutron fluxes. The concrete data are given for the outermost interval of the shielding house. All curves are calculated using the TF-coil model.

layers that are exposed to practically the same neutron flux it is obvious that in this case the Inconel vacuum vessel radiates about a factor of 60 more γ -energy than an assumed stainless steel vessel (AISI 216) does in the cooling time interval of a few days to a few months.

Figure 21 shows the resulting biological dose rate inside the vacuum vessel. For cooling times up to about 100 days the dose rate is nearly constant at 2.5 rem/h, which permits short access to the vacuum vessel (working times up to 1 hour per quarter-year per worker). These working times can, of course, be raised by a factor of 6 if only 2000 discharges of the hydrogen/deuterium type are carried out in one year. Since it is obvious from the analysis in Chapter 3.3 that the Inconel vessel contributes dominantly to dose rates inside the vessel an additional factor of about 60 could be gained by avoiding Inconel in favour of stainless steel⁺).

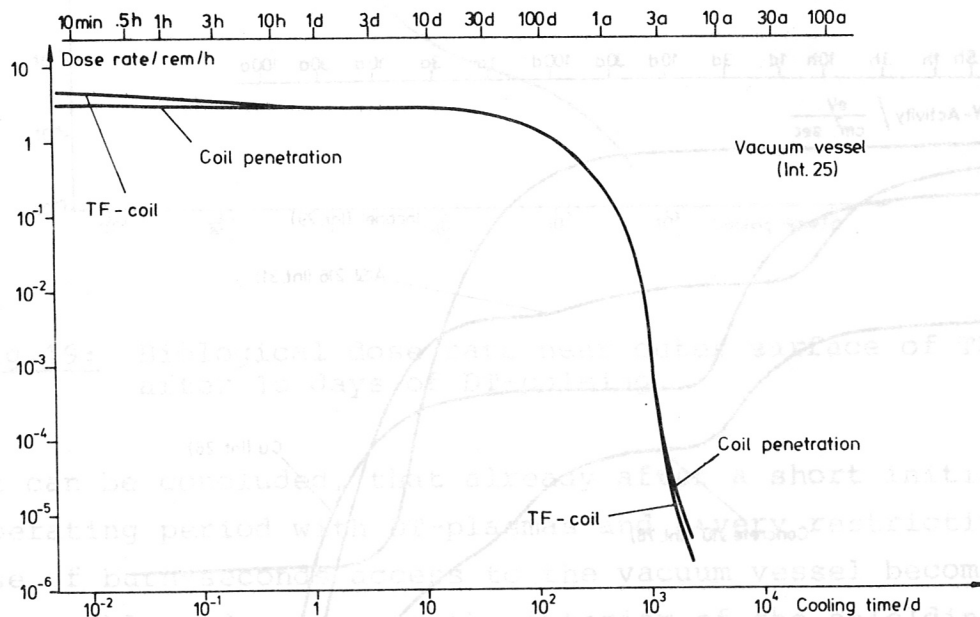


Fig.21: Biological dose rate inside the vacuum vessel after one year of DD-pulsing.

⁺) It appears that the specific combination of high electrical resistivity with favourable mechanical properties of Inconel alloys is unparalleled by any stainless steel. The use of stainless steel thus demands costly trade-offs with other torus components.

Figures 22 and 23 show dose rates outside the TF-coils and outside the shielding house. Outside the TF-coils but inside the shielding house the dose rate in front of a coil penetration allows access for a few hours (1 rem/h). In the coil shadow access appears possible for reasonable working times, even if radiation from near-by penetrations is taken into account. Outside the shielding house even the unoptimised shielding concrete used is sufficient to allow virtually unrestricted access in front of a coil-penetration at less than 10^{-3} rem/h for cooling times greater than 1 hour.

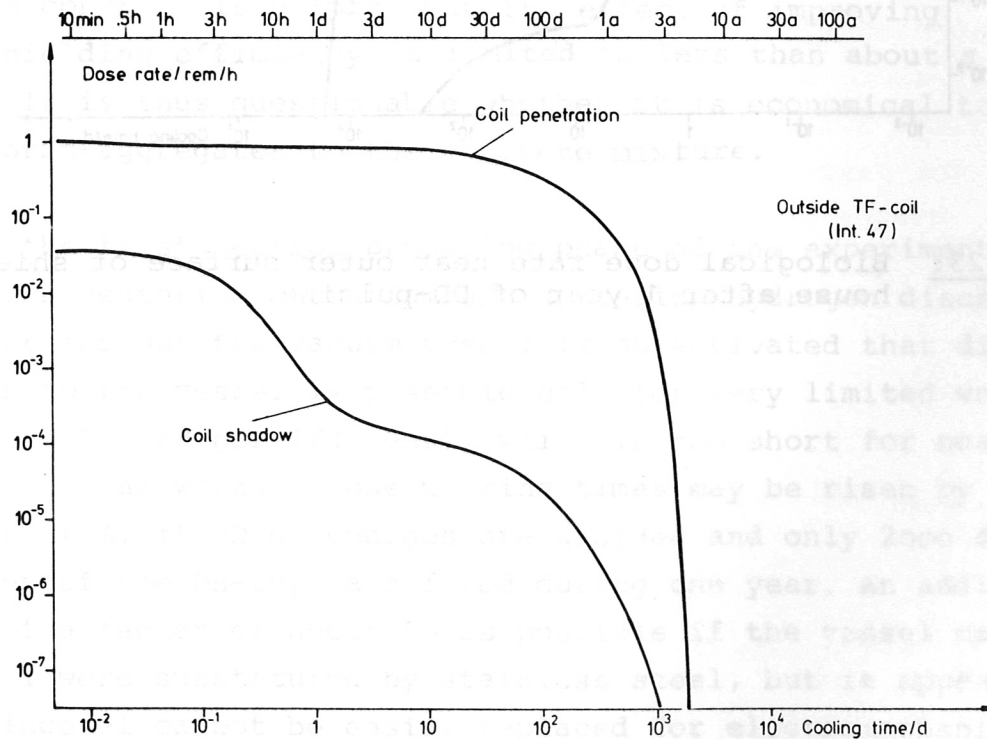


Fig.22: Biological dose rate near outer surface of TF-coils after 1 year of DD-pulsing

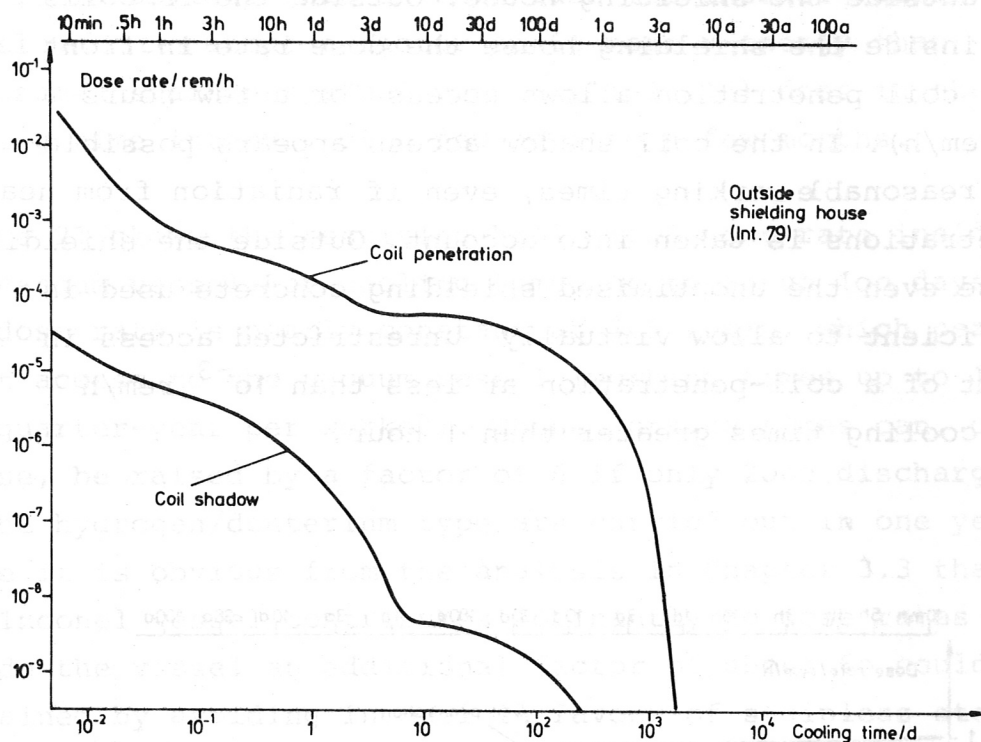


Fig.23: Biological dose rate near outer surface of shielding house after 1 year of DD-pulsing.

6. Conclusions

Within the framework of one-dimensional treatment the nuclear radiation situation during a discharge and after several sequences of discharges has been analysed.

Important findings are that nuclear energy deposition during a discharge is so large, that it plays a significant role in heating the cryogenic apparatus. Shielding the torus with 70 cm of borated concrete, the shielding house, and additional 2 meters of building walls is barely sufficient to reduce prompt radiation doses outside the building to acceptable yearly limits. Adding thermal neutron catchers to the concrete is helpful but the effect of improving the shielding efficiency is limited to less than about a factor of 7. It is thus questionable whether it is economical to add boron-aggregates to the concrete mixture.

After the first neutron producing phase of the experiment, in which deuterium/deuterium and deuterium/hydrogen discharges are carried out the vacuum vessel is so activated that direct access to the vessel is possible only for very limited working times (1 hour per 1/4 year), which is too short for nearly all practical works. These working times may be risen by a factor of 6, if DD-discharges are avoided and only 2000 discharges of the DH-type are fired during one year. An additional gain of a factor of about 60 is possible if the vessel material Inconel were substituted by stainless steel, but it appears that Inconel cannot be easily replaced for electromechanical reasons. The choice of the vessel material is thus decisive for the possibility of realistic hands-on maintenance and repair inside the vessel during the DD- and DH-pulsing phase.

After starting the deuterium/tritium burning, already after a few pulses resulting in a total of 4 burn-seconds access to the vacuum vessel is definitely impossible. Access to the region between TF-coils and shielding house, too, is impossible in front of a TF-coil penetration.

After several years of DT-burning in which 3000 burn-seconds are achieved with a growing duty-cycle of the machine, personal access to the whole area inside the shielding house appears impossible even in the shadow of the TF-coils due to radiation emerging from coil-penetrations. With the shielding concrete chosen, the experiment hall can be entered a few hours after the last discharge for restricted working times. An analysis of the causes of that radiation shows that the radiation results from trace element activation in the shielding house concrete. There are good prospects for improving the accessibility of the experiment area by selecting a better concrete.

The γ -activation of the apparatus after longer cooling times is dominated by Cr^{51} , Co^{58} , Co^{57} and Mn^{54} (half-lives 28 d to 1 a) up to a few years after the last discharge. Then Co^{60} (half-life 5.3 a) remains the dominant source, until after about 100 years Nb^{94} with its half-life of 20.000 years remains. Direct access to the vacuum vessel will not become possible again until after about 20 years of cooling.

References

- /1/ W.W.Engle,Jr.,: A User's Manual for ANISN, Report K-1693, Union Carbide Corp., Nuclear Division, Oak Ridge, Tenn. 1967
- /2/ RSIC Data Library Collection: Coupled 100-Group Neutron 21-Group Gamma-Ray Cross Sections for EPR Neutronics, Contributed by Neutron Physics Division, Oak Ridge National Laboratory, Oak Ridge, Tenn.
- /3/ ICRP Publication 21 in Recommendations of the International Commission on Radiological Protection, ICRP Publications 15 and 21, Pergamon Press.

Appendix A

- /4/ G.Erdtmann, W.Soyka: Die γ -Linien der Radionuklide, Bd.1, Jül-1003-AC, 1973.
- /5/ N.M.Greene et al.: AMPX: A Modular Code System for Generating Coupled Multigroup Neutron-Gamma Libraries from ENDF/B, ORNL-TM-3706, Oak Ridge National Laboratory, 1973.

Concrete 5/5	Si 60.8, Fe 3.4, C 21.3, Nb 1.85, Ta 1.85, Mo 1.0, $\rho = 4 \text{ g/cm}^3$
Concrete 2/6	Fe 60.4, Mn 5.3, Cr 1.9, Ni 2.0, Mo 2.5 (2.9 g/cm^3)
Al-mg	Al 77.0, Mg 2.0 (2.7 g/cm^3)
Concrete 1/10	(by gamma-ray delayed neutron transport calculations) C 35, O 42.5, H 1.5, Mg 2.5, Al 4.5, Si 10.5, S 1.9, Ca 8.7, Ni 0.3, B 0.09, $\rho = 11 \text{ g/cm}^3$
Concrete 1/10	(2.35 g/cm^3) (for determining activation γ -sources) sample is covered with 0.7% by volume of Fe oxide, simulating iron corrosion products
Concrete 1/10	same as 1/10, but for layered concrete, $\rho = 1.8 \text{ g/cm}^3$
Concrete 1/10	C 1.3, Fe 0.3, $\rho = 23.0 \text{ g/cm}^3$
Glass fiber	Si 25.5, C 13.5, Al 7.7, B 2.6, Ca 15.7 (2.5 g/cm^3)
Glass fiber	Fiber 30.0, Glass fiber 30.0 (by volume)
Concrete 1/10	Fiber 30.0, Glass fiber 30.0 (by volume) C 21.6, O 42.5, Ca 42.5 (by volume)
Concrete 1/10	C 42.5, H 7.7, N 0.04, O 0.01 (3.2 $\times 10^{-3} \text{ g/cm}^3$)
N ₂ gas at 30 K	N 100.0 ($4.3 \times 10^{-3} \text{ g/cm}^3$)
Air	N ₂ 80.0, O ₂ 20.0 (by volume) ($1.3 \times 10^{-3} \text{ g/cm}^3$)

Appendix A

Appendix B

Materials

All material compositions are given in weight percentages unless otherwise specified.

<u>Copper</u>	Cu 100.0 (9,8 g/cm ³)
<u>Inconel 625</u>	Ni 60.8, Fe 5.0, Cr 21.5, Nb 1.85, Ta 1.85, Mo 9.0, (8.4 g/cm ³)
<u>AISI 216</u>	Fe 63.4, Mn 8.3, Cr 19.8, Ni 6.0, Mo 2.5 (7.9 g/cm ³)
<u>Al-alloy</u>	Al 97.0, Mg 3.0 (2.7 g/cm ³)
<u>Borated concrete</u>	(for prompt and delayed radiation transport calculations) H 0.55, O 48.5, Na 1.7, Mg 2.5, Al 4.5, Si 30.5, K 1.9, Ca 8.2, Ni 1.2, B 0.39, C 0.11 (2.36 g/cm ³)
<u>Borated Concrete</u>	(for determining activation γ -sources) same as above with 0.2% by volume of Fe added, simulating reinforcement bars.
<u>Ordinary concrete</u>	same atomic composition as borated concrete, except B and C skipped.
<u>Epoxy</u>	C 70.7, H 6.3, O 23.0 (1.3 g/cm ³)
<u>Glass fibre</u>	Si 25.5, O 48.5, Al 7.7, B 2.6, Ca 15.7 (2.5 g/cm ³)
<u>Epoxy/Glass fibre</u>	Epoxy 50.0, Glass fibre 50.0 (by volume)
<u>TF-coil mixture</u>	Epoxy/Glass fibre 15.0, AISI 216 42.5, Cu 42.5 (by volume)
<u>Polystyrol foam</u>	C 92.3, H 7.7, N 0.04, O 0.01 ($3.7 \cdot 10^{-2}$ g/cm ³)
<u>N₂ gas at 80 K</u>	N 100.0 ($4.3 \cdot 10^{-3}$ g/cm ³)
<u>Air</u>	N ₂ 80.0, O ₂ 20.0 (by volume) ($1.3 \cdot 10^{-3}$ g/cm ³)

Appendix B

Activation Reactions and Decay Chains

